University of Zurich[UZH]

UNIVERSITÄT BERN

Fragmentation and Sensitivity Measurements with Comet Interceptor's MANiaC SHU Prototype

Master Thesis in Physics

Lucijana Stanic

Supervised by

PD Dr. Martin Rubin
Daniel Robert Müller

Space Research and Planetary Sciences, Physics Institute, University of Bern

Prof. Dr. Prasenjit Saha

Institute for Computational Sciences, University of Zurich

January 2024

Abstract

The European Space Agency's Comet Interceptor mission is set to launch in 2029. Its aim is to characterise the composition of the surface, the shape and the structure of a dynamically new comet, as well as the composition of its coma. The latter will be analysed using a time-of-flight reflectron mass spectrometer called the Mass Analyser for Neutrals in a Coma, or MANiaC for short. For this work the goal was to test and calibrate a prototype part of the MANiaC, more specifically the Sensor Head Unit (SHU) prototype, using different gases. Static calibrations were performed with the following gases (in order of increasing molar mass) CH_4, Ne, CO, N_2, C_2H_4, Ar, CO_2, C_3H_8, Kr and Xe. Databases were used to compare the recorded mass spectra. In addition, sensitivity measurements were carried out for all gases to enable abundance determination. The measurements indicate that the mass spectra are consistent with the databases for all gases. To meet the requirements the pulser needs to be modified, specifically by reducing the pulser cable capacitance to increase the resolution. Attempting to measure abundances of gas mixtures resulted in differing results with different methods of data analysis. Further experiments are needed to fully understand gas mixture analysis with the instrument in question to determine exact abundances of different gases with similar mass or spectra.

Acknowledgements

Before anything else, I wish to express my gratitude to those who have helped me throughout the process of working and writing this thesis.

I begin by thanking my external supervisor, PD Dr. Martin Rubin, for providing me with the opportunity to work on such an exciting project and for his guidance throughout.

Further I would like to thank Prof. Dr. Prasenjit Saha, for taking on the role as my internal supervisor and for all his counsel from the beginning of my bachelor studies up until the end of my master studies.

Additional thanks to my direct supervisor Daniel Müller, who was an excellent supporter giving me the chance to learn and let me gain my own experience, with endless patience concerning all the questions I had.

Moreover, I extend my appreciation to all individuals associated with the Space Research and Planetary Science Institute in Bern. It has been a pleasure to share offices, engage in interesting conversations and enjoy coffee breaks with you.

Lastly, I express my heartfelt gratitude to my friends and family for their unwavering support throughout my academic journey so far.

Contents

Part I
Introduction & Theory

The focus of this thesis is the mass spectrometer slated for installation on the Comet Interceptor spacecraft, set to launch aboard Ariane 6 alongside the ARIEL space telescope in 2029. This marks a significant milestone as it represents the first in situ study of a dynamically new comet, offering a novel perspective on their composition and appearance.

To grasp the significance of this mission within the realm of cometary science and to introduce mass spectrometers, this chapter will commence with an overview of the current understanding of comets. Subsequently, it will delve into the Comet Interceptor mission and its specific objectives. Additionally, the chapter will provide an introduction to mass spectrometry, followed by a detailed explanation of the key features of the mass spectrometer designated for the Comet Interceptor mission.

1 Cometary Science

1.1 Observation of Comets

For a long time, humans around the world have been fascinated by the appearances of comets. Many old scriptures contain descriptions of big glowing balls of fire gliding across the sky. The apparition of comets was often ascribed a supernatural meaning by various cultures.

Although not all questions about comets are answered, we have more knowledge about them than our ancestors did, for instance we can make out and define different parts of a comet. Each comet has three main elements: the nucleus, which is the solid core typically few kilometers in diameter and composed of rock, dust, frozen water, carbon dioxide, ammonia, and methane among others; the coma, which is the dust and gas envelope around the nucleus, usually spreading tens of thousands of kilometers in diameter; and finally, the tail, which can further be divided into ion, neutral gas and dust tail, the ion tail being illuminated from ionisation, while the latter two reflect the sunlight directly, and can be hundreds of millions of kilometers in length. The mentioned parts can be seen in figure 1.

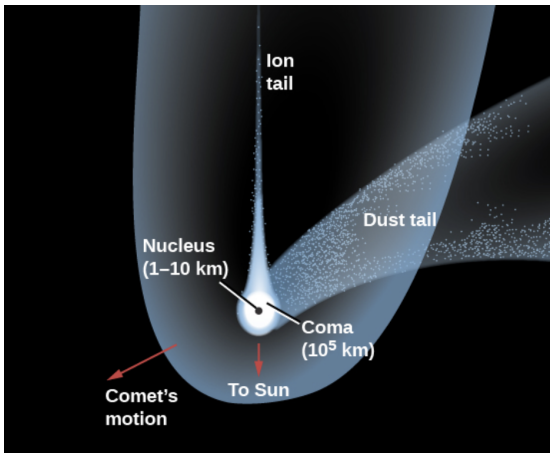

Figure 1: The different parts of a comet (not to scale) include nucleus, coma and tail. The tail can be further divided into the dust tail and the ion tail. Taken from [1].

Most knowledge about comets was acquired in the last 100 years, especially during the last few decades. The contemporary framework that explains the physical and chemical characteristics of comets has its origins in the 1950s work of Fred Whipple [2]. Before Whipple, many astronomers believed that the nucleus of a comet was a cluster of solids. Whipple suggested that it was probably a solid body measuring only a few kilometers across, composed mostly of water ice with additional ices mixed with silicate grains and dust. This concept has been referred to as the "dirty snowball" model and has remained a reliable description for most comets.

The most straightforward means to investigate comets is to dispatch spacecraft within close proximity, as the nuclei are usually too small and dark, and therefore too faint, to be observed and studied in detail from Earth. In 1985, the International Cometary Explorer (ICE) passed through the tail of the 21P/Giacobini-Zinner comet in the first-ever comet encounter [3]. The first deep space mission of the European Space Agency was Giotto which captured the closest images taken of a comet. It flew past the nucleus of comet 1P/Halley [3]. The Rosetta mission of 2014 [4] was by far the most fruitful examination of a comet, with the spacecraft becoming the first to follow, orbit and land on a comet. The main goal of the mission was to learn more

about the physical and chemical composition of comets, to observe the nucleus more closely as it covered a range in heliocentric distance and substantially changed its outgassing and dust production, and to place these findings in the context of the history of our solar system.

1.2 Comet Interceptor

Almost all of the missions that have been developed to explore comets have targeted short-period comets, i.e. comets with an orbital period around the Sun of less than 200 years. The reason for this is obvious: one knows that the comet is coming, and one can predict its trajectory and speed. Halley's comet is a prime example, having been observed and documented at least since 240 BC [5]. The comet's appearances and reappearances were further investigated and understood by Edmund Halley [6]. This insight was used to enable the Giotto mission on Halley's latest pass.

Despite the advantage of being able to prepare for such an encounter well in advance, there is a downside. Such short-period comets have usually completed many orbits and come close to the Sun many times, causing them to undergo enormous morphological, compositional and chemical changes [7]. As a result, any information they might have given us about the initial composition at the birth of our Solar System is hampered. If one wanted to study the compositional and isotopic ratios further, a more pristine comet would have to be studied.

This is the aim of ESA's Comet Interceptor mission, which will target an as-yet-unidentified object to be chosen once the mission is close to launch or already in space [8]. It will be the first mission to aim for a dynamically new comet (DNC), i.e. a comet entering the Solar System for the first time. It will take advantage of the launch of the ARIEL mission, scheduled for 2029, and will target the stable Sun-Earth L2 point for a parking position before beginning the journey to the interception point.

Based on estimates of previously found Long Period Comets (LPCs), it will spend up to 2-3 years waiting for a DNC that it can target at a reasonable speed and trajectory. Including travel and flyby, the mission will last less than five years. If no target is found, which is highly unlikely, there is a back-up of short period comets to study. On the more optimistic side, there is also a very small but non-zero chance of encountering an interstellar object (ISO) such as 1I/'Oumuamua and 2I/Borisov, which would be of great scientific interest.

The mission will comprise three parts: one main spacecraft (S/C A, contributed by ESA) and two smaller probes (S/C B1 and B2, contributed by ESA and JAXA respectively). S/C A will perform the flyby at a greater distance than B1 and B2. This configuration with multiple spacecrafts is a precautionary measure since expectations for the activity levels of a DNC are estimated to be high and unpredictable, involving coma passage and collisions with dust grains at speeds ranging from 10 to 70 kms^{-1}. S/C A will execute the entire maneuver from a safe distance of 1000 km from the nucleus, while B1 and B2 will approach the comet at a hazardous but potentially lucrative closer range, risking not surviving the whole encounter. A figure showing the fly-by can be seen in figure 2.

The spacecraft's payloads comprise nine distinct instruments, such as a high-resolution camera, an IR multi-spectral imager, a polarimetric camera, and a mass spectrometer. The main objective is to obtain data on the morphology, composition, and plasma environment of the comet at a unique point in its evolution that has not been measured for any other comet.

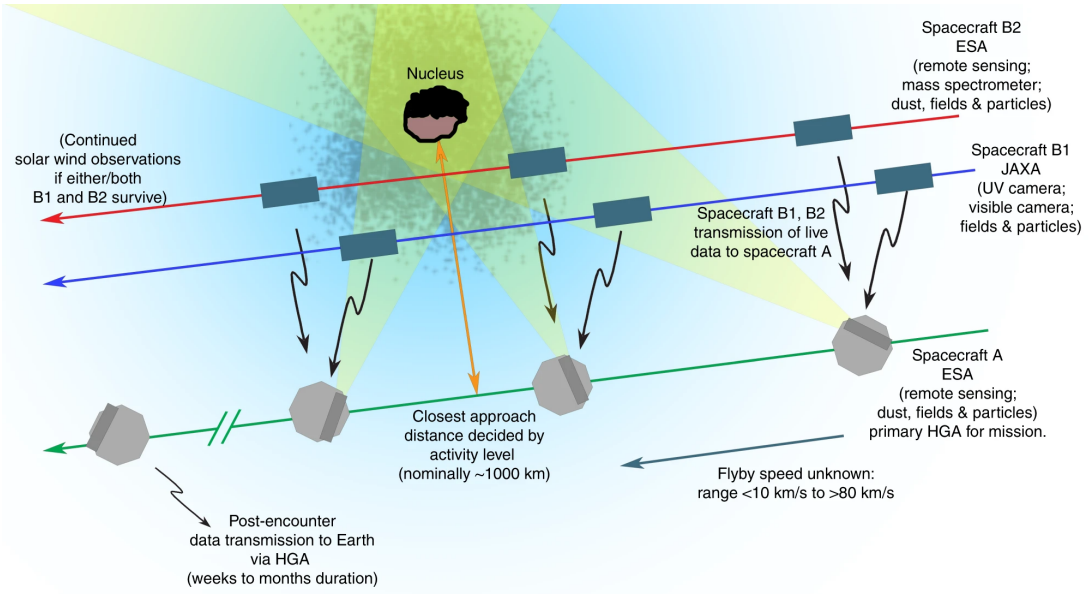

Figure 2: The planned scenario on how Comet Interceptor will approach the target with its three spacecrafts. Instruments carried by each are written in brackets. Taken from [8].

1.2.1 Mass Analyser for Neutrals in a Coma

The Mass Analyser for Neutrals in a Coma (MANiaC) is compromised of a time-of-flight mass spectrometer (ToF-MS) and a neutral density gauge (NDG). The mass spectrometer can analyse the relative abundances, while the NDG measures the absolute gas density. By combining these measurements, absolute densities of volatiles during the fly-by can be determined. The main scientific objectives of MANiaC are to provide answers to the following questions [9]:

- Measure the abundances of the major volatiles, H_2O, CO_2 and CO, and compare them with numbers obtained from Earth-based observations.
- Determine the deuterium-to-hydrogen ratio in H_2O.
- Obtain measurements of other key volatiles, such as O_2, and compare their abundances to those found in other comets
- Study (complex) organic molecules and other species that may be important in prebiotic chemistry.
- Measure the composition and abundance of icy grains in the event that some of these are captured.

2 Mass Spectrometry

2.1 General

A mass spectrometer (MS) is a scientific instrument used for analysing samples. It transforms the sample into a gaseous stream of ions and sorts them based on their mass-to-charge ratio, generating a mass spectrum. This spectrum allows for the determination of not only relative, but also absolute component abundances when supplemented by additional sensitivity measurements. Each and any MS will contain the following five components:

1. A device functioning as an inlet system for inserting the probe.
2. An ion source component.
3. One or multiple analysers, under vacuum, are employed to separate ions based on their m/z ratio.
4. A detector for measuring the quantity and position or arrival time of the ions successfully passing the analyser section.
5. A computer which will receive and process the data to create a mass spectrum.

2.2 Ionisation

The first step in the analysis of compounds in a MS is the production of corresponding gas phase ions. Ions are positively or negatively charged atoms, groups of atoms or molecules. This process of ion generation (also called ionisation) enables a MS to measure both cations (positive ions) and anions (negative ions). Some of the ionisation methods include electron ionisation, chemical ionisation, electro spray ionisation, and laser desorption.

In order to ionise a molecule, a specific ionisation energy is required. The first ionisation energy is the minimum energy required to remove an electron from the highest occupied orbital in the electronic ground state of a neutral particle, be it an atom, radical or molecule. To remove further electrons from higher energy states, the required energy is known as the second ionisation energy, and so on. This unit of energy is typically measured in electronvolts (eV), where 1 eV corresponds to the energy that an electron gains by passing through a potential difference of 1 V. The majority of elements demonstrate ionisation energies that range between 5 and 20 eV, while organic molecules usually fall between 8 to 13 eV [10].

2.2.1 Electron ionisation

As the MANiaC employs electron ionisation, this work will solely focus on this method of ionisation.
To apply ionisation energy to a molecule, various techniques are available. For gas phase samples, the electron ionisation (EI) is a highly effective technique, previously called electron impact ionisation. This method involves inducing an electron beam perpendicular to the stream of molecules using a heated filament. Electrons are emitted from the cathodic filament and travel towards the anode, which acts as the electron discharge. A simplified depiction of an ion source region can be observed in figure 3. The ion source region of the MANiaC SHU is depicted in figure 4. The potential difference in our case, as well as many others, is 70 eV. This results in electrons having a kinetic energy of 70 eV, which is typically enough to ionise most molecules, leading to extensive fragmentation. Fragmentation is the process by which ions are broken down into smaller fragments.

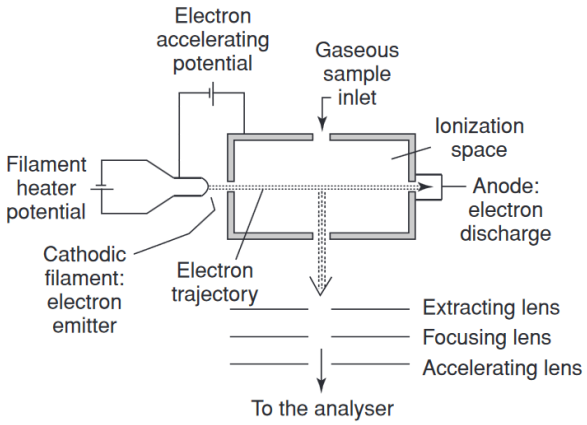

Figure 3: Scheme of electron ionisation. Taken from [11].

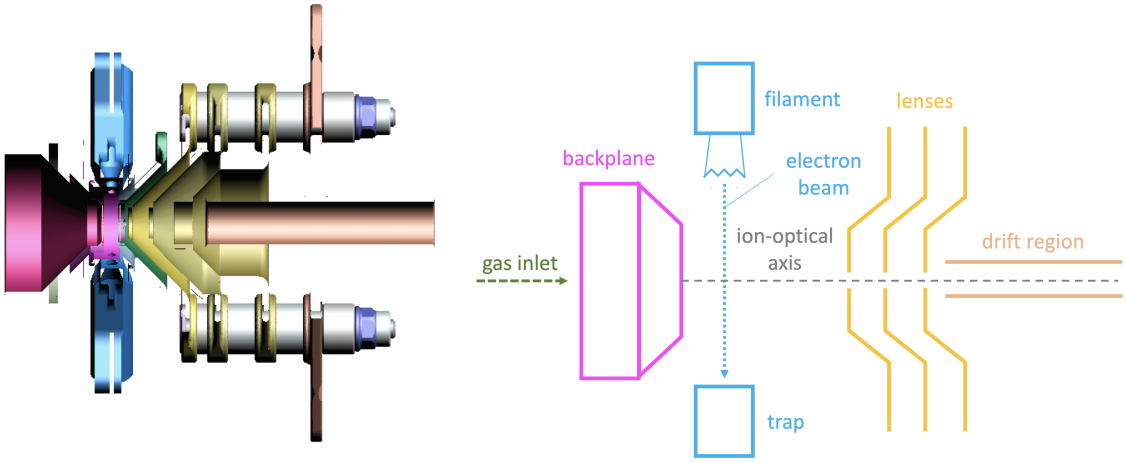

(a) 3D-Drawing (b) Schematic depiction

Figure 4: Ion source region of the MANiaC SHU.

2.3 Time-of-Flight Mass Spectrometry

A Time-of-Flight mass spectrometer (TOF-MS) operates by applying an electric field to the ions in the ion source region. The electric field accelerates the ions with equal acceleration through a drift tube. As the ions have varying masses, their flight time will differ accordingly, and they will arrive sequentially at the detector. By measuring this time, one can infer their masses as follows: An ion with the mass m and charge q will travel through an electric potential E_{el}. By equating the potential energy of the field and the kinetic energy of the ion, we can discern

$$\begin{aligned} qE_{\text{el}} &= \frac{1}{2}mv^2 \\ \Rightarrow v &= \sqrt{\frac{2qE_{\text{el}}}{m}}. \end{aligned} \tag{1}$$

If the distance that the ion needs to traverse is d, then:

$$t = d\sqrt{\frac{m}{2qE_{\text{el}}}}. \tag{2}$$

If all parameters remain equal, the ion with the lower mass will move faster and traverse the distance between the ionisation region and detector more quickly. To calculate the mass-to-charge ratio from the time-of-flight, one should employ the formula:

$$\frac{m}{q} = \frac{(t_i - t_0)^2}{C}. \tag{3}$$

C and t_0 are constants that can be obtained by identifying at least two peaks in the spectrum, while t_i is the measured arrival time at the detector. In particular, t_0 is the effective start time and includes any delay that originates in the measurement electronics.

There are several advantages to this mass spectrometer compared to others. One of them is its straightforward construction and the fact that it only requires two reference points to measure. Another advantage is that all the ions are produced simultaneously, unlike certain scanning analysers that sequentially transmit one mass-per-charge after the other. A single spectrum is acquired within a matter of tens of microseconds, allowing for several thousand spectra to be accumulated and integrated in approximately one second.

2.3.1 Reflectron Time-of-Flight Mass Spectrometer

To achieve a higher mass resolution, the notion of which will be discussed further in 2.4.3, one can use a Reflectron-TOF-MS (RTOF) instead of a linear TOF-MS. The RTOF-MS has an added component of a retarding field, which serves as an ion mirror by accelerating and deflecting ions backwards into the detector. The mirror typically comprises a series of ring electrodes that extend the flight path without increasing the size of the instrument significantly, which is a good side-effect since it leads to the extension of time for separation. However, higher mass resolution may occasionally be counterbalanced by a loss of sensitivity if ions are lost or if the flight time reduces the extraction frequency. Nevertheless, these should be minor issues for MANiaC.

The explanation of how the reflectron enhances the mass resolution is demonstrated in figure 5 and can be derived as followed (from [11]): Assuming two ions of equal mass possess differing kinetic energies, denoted as $E_{\mathrm{k},1}$ and $E_{\mathrm{k},2}$, with a^2 representing the ratio between them:

$$\frac{E_{\mathrm{k},2}}{E_{\mathrm{k},1}} = a^2 \tag{4}$$

As a result, their velocities along the x-axis in the field-free area will differ,

$$\begin{aligned} v_{\mathrm{x},1} &= \sqrt{\frac{2E_{\mathrm{k},1}}{m}} \\ v_{\mathrm{x},2} &= \sqrt{\frac{2E_{\mathrm{k},2}}{m}} = \sqrt{\frac{2E_{\mathrm{k},1}a^2}{m}} = a v_{\mathrm{x},1} \end{aligned} \tag{5}$$

leading to varying traversal times in the field-free regions outside of the reflectron with the total path L

$$\begin{aligned} t_1 &= \frac{L}{v_{\mathrm{x},1}} \\ t_2 &= \frac{L}{v_{\mathrm{x},2}} = \frac{L}{a v_{\mathrm{x},1}} = \frac{t_1}{a} \end{aligned} \tag{6}$$

Subsequently, the ions reach depths of d_1 and d_2 respectively upon entering the reflectron.

$$\begin{aligned} d_1 &= \frac{E_{\mathrm{k},1}}{qE} \\ d_2 &= \frac{E_{\mathrm{k},2}}{qE} = a^2 \frac{E_{\mathrm{k},1}}{qE} = a^2 d_1 \end{aligned} \tag{7}$$

with E the electric field in the reflectron region. They remain in the reflectron for durations $t_{r,1}$ and $t_{r,2}$

$$\begin{aligned} t_{r,1} &= \frac{4d}{v_{x,1}} \\ t_{r,2} &= \frac{4d}{v_{x,2}} = \frac{4a^2 d_1}{a v_{x,1}} = \frac{4ad}{v_{x,1}} = a t_{r,1} \end{aligned} \tag{8}$$

Ultimately, the total flight time of both ions can be calculated:

$$\begin{aligned} t_{tot,1} &= t_1 + t_{r,1} \\ t_{tot,2} &= \frac{t_1}{a} + a t_{r,1} \end{aligned} \tag{9}$$

We observe that the fluctuations in the total flight duration balance each other out, leading to a compensation effect of the different kinetic energies.

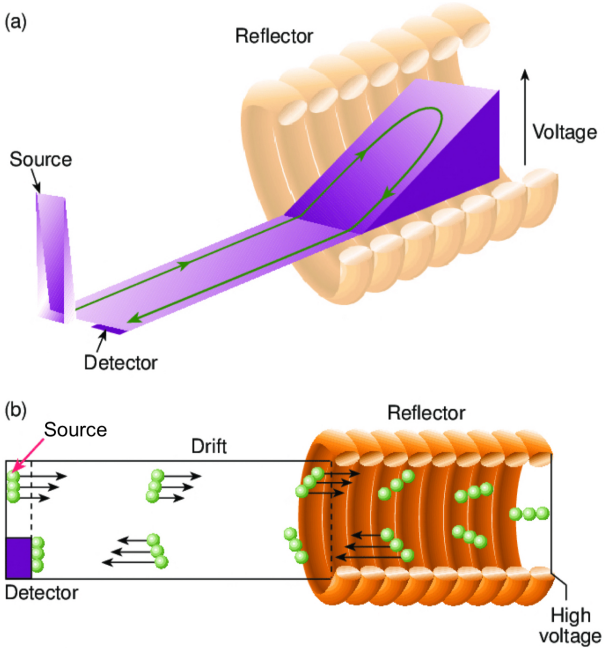

Figure 5: The principle of the RTOF is illustrated in the two images above. Image (a) displays the potential gradient in the reflector section, while image (b) shows that particles with equal mass but different kinetic energies reach the detector simultaneously. This is due to more energetic particles traveling further inside the reflectron and thus taking longer to reach the detector despite having a higher speed. Taken from [12].

In figure 6a a schematic depiction of a RTOF-MS can be seen, in comparison to the 3D drawing of the MANiaC SHU in figure 6b.

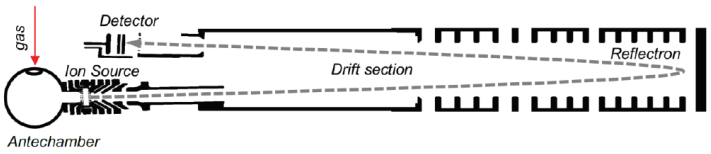

(a) Schematic depiction. Taken from [13].

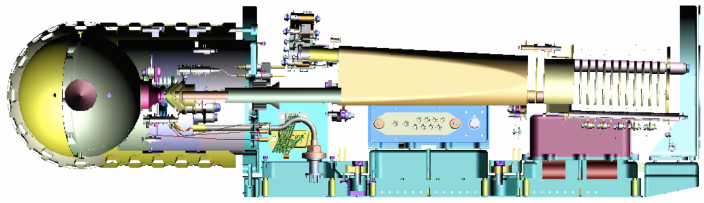

(b) 3D-Drawing.

Figure 6: Two ways to illustrate the MANiaC SHU instrument. It consists of five main parts: the antechamber, which serves as an entry point for molecules and allows for thermalisation before entering the ion source region; the ion source region itself; the drift tube; the reflectron; and finally, the detector. The order of the mentioned components is the order in which ions travel through the mass analyser.

2.3.2 Detector

The electron multiplier (EM) is one of the most commonly used ion detectors in mass spectrometry. To detect ions coming from the drift region, they are accelerated to high velocity by applying a conversion dynode opposite to the charge of the ions used. The ions then strike the dynode, causing the emission of electrons. This whole process results in an amplification of the original signal that would have been produced by the original ion, and can lead to a gain of up to 10^6.
For the MANiaC, two microchannel plates (MCPs) in series are used, which are an arrangement of channels made up of resistive material, each forming a miniature electron multiplier. The components are arranged in a chevron shape, angled slightly and parallel to each other. This design reduces ion feedback and increases gain at a specific voltage. In figure 7 a schematic depiction of the whole process is shown.

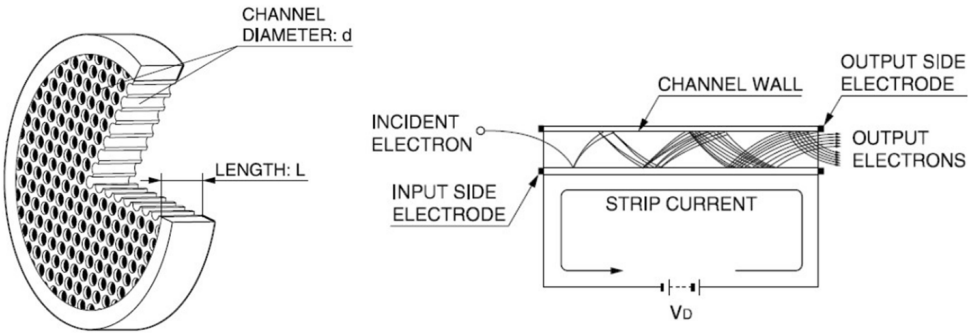

Figure 7: Schematic diagram of how an MCP works. The ions enter the tubes and hit the walls as the channels are slightly angled. This impact triggers a cascade of electrons which propagate through the channels, guided by the strong electric field applied and becoming amplified by many orders of magnitude. The MANiaC detector is composed of two MCP plates arranged in series with angled channels forming a chevron shape. Taken from [14].

2.4 Analysing the Spectrum

The nature and structure of a compound can be derived from the spectrum. If the compound is pure, the spectrum may be compared to reference spectra from databases, which typically include recordings of the pure compound. But, when multiple substances are present in the compound, the analysis becomes considerably more intricate and requires a deeper investigation. Apart from that, there are few molecules that exclusively lead to one type of ion, most compounds create a non-trivial mass spectrum. Analysing such spectra is a skill that requires specific attention, particularly in the field of organic chemistry.

2.4.1 Fragmentation Patterns

When a molecule loses an electron, an ion is formed. If more energy than required is applied to remove the first electron, fragmentation will occur, which in the case of the MANiaC SHU is almost always the case. This breaks the molecule ion into product ions or so called fragments. The original compound's abundance will decrease, and signals will appear at m/z values where none were expected in the unionised state (see figure 8a).

This phenomenon could have a positive or negative impact on the evaluation. On one hand, the presence of additional peaks may obscure the signals of other compounds that would have been visible at the mass-to-charge ratio where the fragments emerge. Additionally it creates an uncertainty on the overall abundance estimations, since with each supplementary peak, there is an augmented uncertainty due to decrease in peak heights and hence lower signal-to-noise ratios.

On the other hand, if a compound possesses reference mass spectra in the literature or, even better, one has performed calibration measurements with a pure compound, the distinctive fragmentation pattern of a particular molecule can be retrieved and used to identify it accordingly. It is particularly valuable in organic chemistry, where it is a frequent occurrence for two molecules with the same atomic weight but vastly different structures to result in distinct fragmentation patterns. This can be used as a kind of molecular fingerprint to identify them in a crowded spectrum, greatly improving analysis, even if the parent ions cannot be separated.

On another note, reducing the fragmentation patterns could be achieved by exclusively employing the minimal amount of ionisation energy necessary to ionise the molecule, despite the above mentioned advantage. For the majority of organic molecules, 10 eV is adequate for ionisation, whereas excess energy leads to extensive fragmentation. By utilising the minimum amount, fewer fragments are formed, subsequently allowing for improved detection of the molecular parent ion. But in this scenario the number of ions detected is reduced, with a decrease in intensity due to lower ionisation efficiency at lower electron energies, as shown in figure 8b. A broad maximum appears around 70-100 eV. Higher energies will cause a decline in the number of ions produced since the effective wavelength becomes progressively shorter, reducing the likelihood of interactions with another electron. This is the reason why the standard electron ionisation mass spectrometer usually uses 70 eV to ionise the sample.

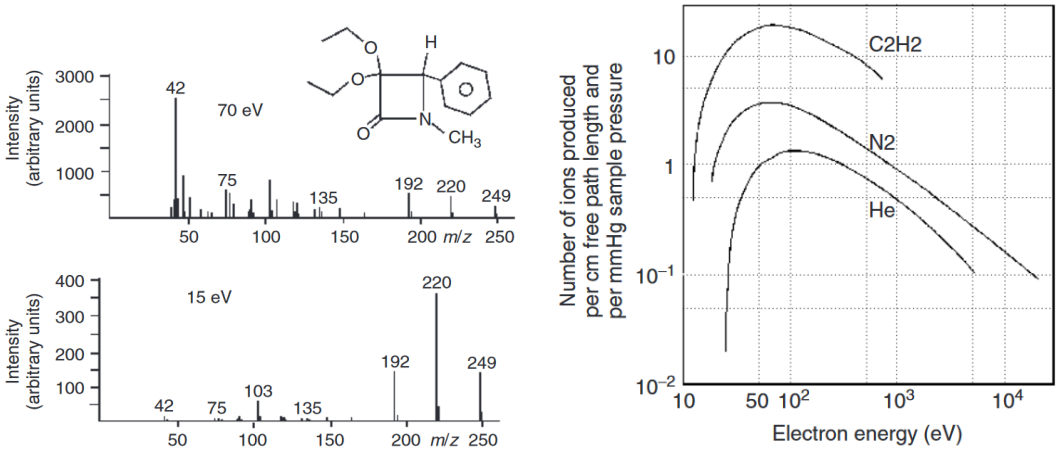

(a) (b)

Figure 8: The effects of higher or lower energies applied. In (a) two spectra of the same organic molecule but at different beam energies are shown. One can observe less fragmentation with a lower energy but also less intensity of the arrived ions as can be read off on the y-axes. In (b) we see that the number of ions produced as a function of electron energy reaches a maximum at around 70 eV. Taken from [11].

2.4.2 Isotope Ratios

Another important part of spectrum analysis is the study of isotope patterns. Here we focus on stable isotopes, as unstable isotopes, such as ^{26}Al, have not yet been observed in the gas phase around comets. The separation of masses by m/z leads to the separation of the natural isotopes and thus to the appearance of two or more peaks for a chemically pure substance containing elements with two or more stable isotopes. Statistical methods are usually used to calculate the expected isotopic pattern, since the appearance of different isotopes depends on the abundance of that isotope and therefore the probabilities with which certain m/z will appear in the spectrum can be determined. To illustrate this, the example of chlorine is taken, which has two isotopes $[^{35}\text{Cl}]$=75.5% and $[^{37}\text{Cl}]$=24.5%. The pattern for the Cl_2^+ ion can be calculated with the results shown in table 1.

Cl_2^+ combinations	**m/z**	**intensities ($\sum = 1$)**			**normalised**
$[^{35}Cl_2]^+$	70	0.755^2=0.570		0.570	100.0%
$[^{35}Cl^{37}Cl]^+$	72	0.755·0.245=0.185	intensities add up	0.370	64.9%
$[^{37}Cl^{35}Cl]^+$	72	0.245·0.755=0.185			
$[^{37}Cl_2]^+$	74	0.245^2=0.060		0.060	10.5%

Table 1: Isotope pattern for Cl_2. Intensities usually get normalised to the most abundant isotope ion, which in this case would be $[^{35}Cl_2]^+$

In general, to determine the pattern of a molecule with n atoms of an element X with the isotopes A_X, B_X, ... and the corresponding isotope abundances I_{AX}, I_{BX}, ... one can use the following:

$$(I_{AX} + I_{BX} + ...)^n \tag{10}$$

If the molecule consists of several types of atoms X, Y, Z, ..., then the intensity distribution is as follows:

$$(I_{AX} + I_{BX} + ...)^{n_X} \cdot (I_{AY} + I_{BY} + ...)^{n_Y} \cdot (I_{Az} + I_{BZ} + ...)^{n_Z} \cdot ... \tag{11}$$

A depiction of such a pattern for chlorine and bromine can be seen in figure 9.

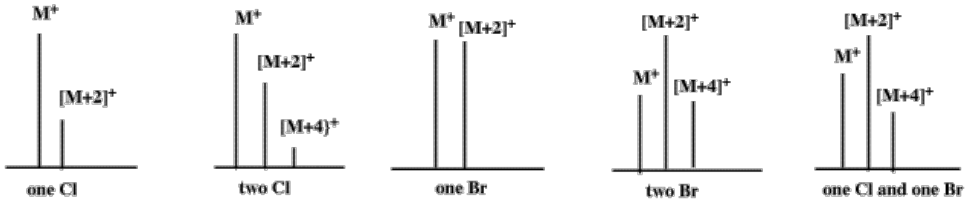

Figure 9: Isotope patterns of the combinations of chlorine and bromine as histograms. Taken from [15].

2.4.3 Resolution

Up to this point, we assumed that the nominal masses would be sufficiently spaced apart to be accurately detected. However, this is not always the case and depends on the resolving power of the mass spectrometer and the resolution of the mass spectrum. There are various methods to define these quantities. In the subsequent thesis, we will apply the definition outlined in the IUPAC Gold Book [16], which is as follows:

$$\begin{aligned} R &= \frac{M}{\Delta M} = \text{resolution} \\ \Delta M &= \text{peak width at a given height} \\ M &= \text{center mass of the corresponding peak} \end{aligned} \tag{12}$$

The higher the resolution, the greater the peak separation and subsequently, the more accurate the mass determination. The spectra of peaks with higher resolution compared to lower ones can be seen in figure 10.

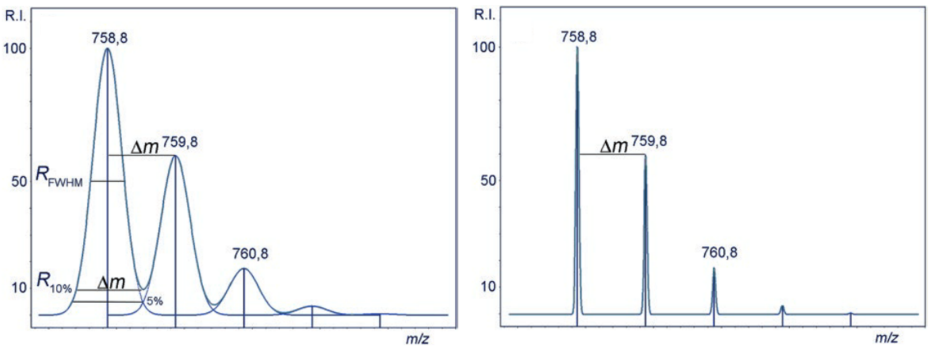

Figure 10: Comparison of higher and lower resolution peaks with the molecule ion $C_{54}H_{110}$. The spectrum on the lefthand side has a resolution of $R_{10\%} = 760$, sufficient to distinguish between the nominal masses, while the one on the righthand side has ten times higher resolution. Taken from [17].

The minimum peak separation or resolving power can be defined in various ways. One approach involves using the peak width definition, where the width of the peak is measured at a particular fraction of its height, whether that is 0.5%, 5%, 10%, or 50%. The last of these, known as the Full-Width-Half-Maximum (FWHM), will be utilised in this work.

Part II
Experiments

This part is dedicated to the experimental aspects. Section 3 introduces the SHU prototype setup, followed by an elaboration on the preparations for every measurement in section 4. Section 5 discusses the ion simulation software SIMION, while summarising the comparison between simulations and the actual measurements. Data analysis and processing applied to each measurement is explained in section 6. A brief outline of the primary fragmentation and isotope pattern analysis is presented in section 7, utilising methane and xenon as case studies. The enhancement of the signal induced by some modification around the devices connected to the instrument is presented in 8. Additionally, the sensitivity of all gases within the laboratory was measured and studied, to which the results can be found in section 10. In certain instances, molecules may possess identical mass-per-charge ratios and/or interfering fragments, which can impede analysis. Sensitivity relations can be measured to determine the contributions of each product peak from a molecule and to estimate their abundances. These measurements and their discussion can be found in sections 11 and 12.

3 Setup

The experimental setup comprised several components, which are described in the following paragraph and shown in figure 11 for better illustration and overview. Two vacuum pumps were responsible for evacuating the chamber; namely, one preliminary pump and one turbo pump, to reach low pressures. Initially, there was only one inlet for a gas bottle. However, a valve was later installed to enable two bottles to be attached, providing a means to create gas mixtures. Two power supplies were used, one for the pulser and one for the filament controller. An arbitrary function generator produced the trigger signal necessary for the pulser. Two setups were generally employed for the pulser: the primary installation involved placing it inside the chamber along with the mass spectrometer, aligning with the mission's intended configuration. In cases where issues arose with the pulser or repairs were necessary, a backup pulser could be installed externally and connected through chamber feedthroughs. Additionally, there was a controller for the filament current, ensuring a approximately constant emission of electrons. The Multichannel-Power-Output-Device (MPOD) served as an external power source connected to the computer allowing for optimised control of the low voltage (LV) and high voltage (HV) sets, resulting in an optimal flight path for the ions. To read the detector signal, the *Acqiris* card together with its software *Acqiris Live* were used.
An image of the MANiaC SHU prototype as well as the pumping station setup can be seen in figure 12.

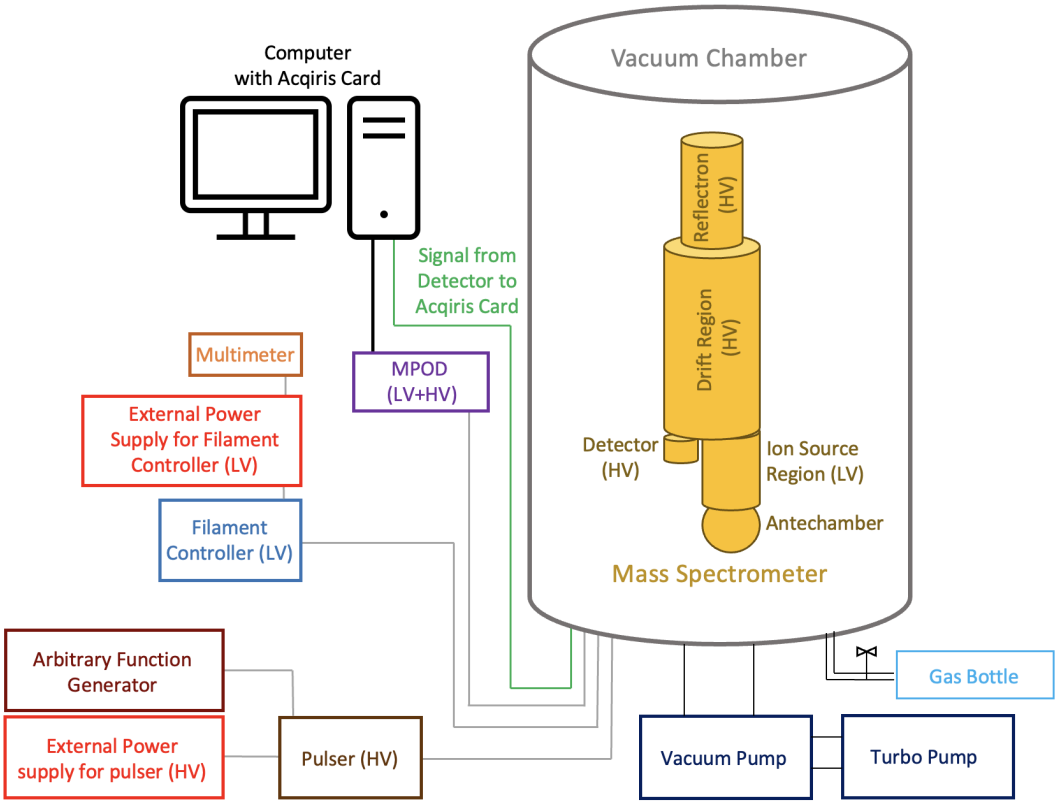

Figure 11: Schematic depiction of setup.

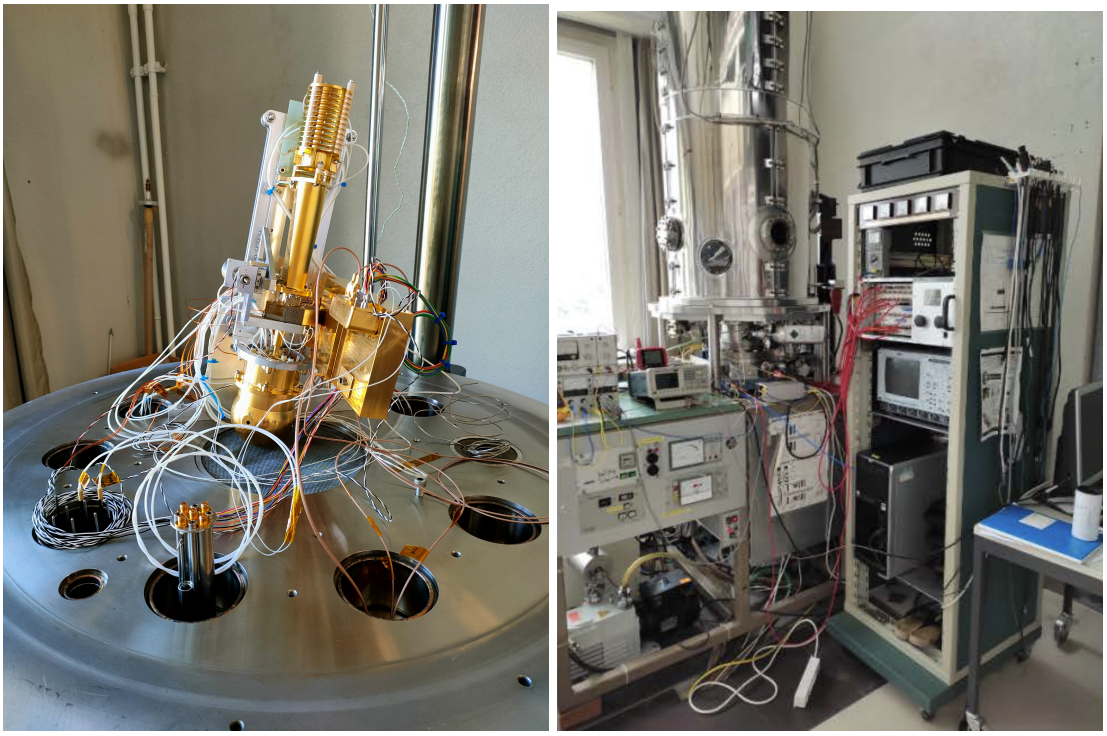

(a) MANiaC SHU prototype. (b) Setup in person, taken from [18].

Figure 12: MANiaC SHU prototype and pumping station.

4 Preparations

Before any measurements wereto be carried out with the MANiaC SHU prototype there was a lot of preparation to be done. Following the installation of the mass analyser or any changes made to its setup, a specific sequence of steps must be taken before measurements may be performed. These steps include pumping, heating, turning on external components, conditioning and optimising. A detailed description, can be found in the *"Pumpstation-5 and SHU User Manual"* written by Boris Pestoni [18].

Pumping: The first step after closing the chamber with the instrument inside is to evacuate it using two vacuum pumps, a regular one and a turbo pump. Both pumps are necessary to reach the desired pressure level, ideally below 10^{-7} mbar, since high voltages should not be used to operate the MCP if the pressure exceeds 10^{-6} mbar. Additionally, one aims to remove any leftover gases ideally. Unfortunately, some nitrogen, oxygen or water will usually remain in the gas chamber, regardless of how long it has been pumped. This is due to the difficulty of achieving a complete seal.

Heating: To remove any residual water or other volatile substances from the surfaces inside the chamber, it is customary to heat it up to 80°C and allow it to bake out for approximately 36-72 hours.

Turning on External Components: After allowing the chamber to cool down again after heating, it is time to switch on all the external components. There is the external power supply, which is responsible for supplying power to the pulser, as well as the arbitrary function generator, which generates the necessary trigger signal for the extraction of the ions. Additionally, the pulser, previously utilised in a configuration inside the chamber, must also be activated. Then there is a controller for the filament current, which regulates the amount of current passing through the filament in the ionisation region (see figure 3) and measures the effective emission current. Finally, the MPOD crate must be switched on, which is the power supply that allows the low and high voltages to be controlled by the computer.

Conditioning: Every time the mass analyser and MCP detector are exposed to air, they require conditioning. This involves slowly and gradually increasing the voltage until the desired MCP operating voltage is reached.

Optimising: To determine the optimal voltage set for directing most of the ions into the detector, voltage set optimisation is performed beforehand. For details on the optimisation algorithm, refer to André Bieler's PhD thesis [19]. Roughly speaking, the script assesses a target function - in our case, an evaluation of the height and area of a peak found within the selected range. It assesses the function for different voltage sets and consequently tries other voltage sets based on this assessment until the optimal voltage set, in our particular instance, with maximum area and maximum height, is found.

5 SIMION

To gain insight into the ions' behaviour during its flight path it is common to use SIMION; an ion optics simulation program developed in the 1970s [20] that calculates ion trajectories in electric fields when voltages are defined for electrodes. It is now a widely used simulation program in both academia and industry.

At the outset, one of the objectives was to evaluate certain voltage sets obtained from the optimisation program and examine whether SIMION-generated voltage sets could produce better practical outcomes. Regrettably, the study proved unsuccessful. In fact, the optimal voltage sets identified by the optimisation script resulted in only around 50% of ions colliding with the walls in front of the detector, as illustrated in figure 14, and getting lost. Additionally, the voltage configuration that proved effective in SIMION simulations, resulting in all ions reaching the detector (see figure 13a), was found to be impractical in reality. This can be attributed to the configuration of the ion source (refer to figure 3). For this specific set, the filament housing would have a positive voltage applied to it, which would cause the electrons emitted by the filament to be diverted towards it and not ionise any molecules. This part was not considered in SIMION as the positive ions were placed simply in the ion source region without requiring electron ionisation beforehand.

Apart from the problem of not taking the ionisation process into account, SIMION has several limitations, such as the use of ideal grids, the neglect of the effects of surface contamination on electric fields, the lack of consideration of machining and assembly tolerances as well as the frequent exclusion of space charge. Hence it is important to note that SIMION aims to evaluate the feasibility of the 'ideal' ion trajectories. However, the optimised voltages may deviate from the simulation results.

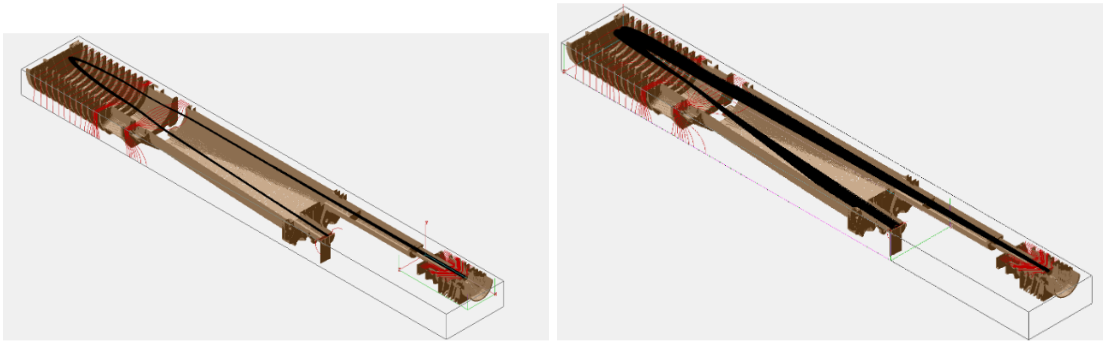

(a) (b)

Figure 13: The ionised molecules' trajectories are visible and may be compared in these two images. Image (a) displays the nominal voltage set found using SIMION, while image (b) shows the optimised voltage set from the prototype in the lab. The nominal voltage set appears to be the optimal choice based on SIMION simulations alone, however experimental tests have shown otherwise.

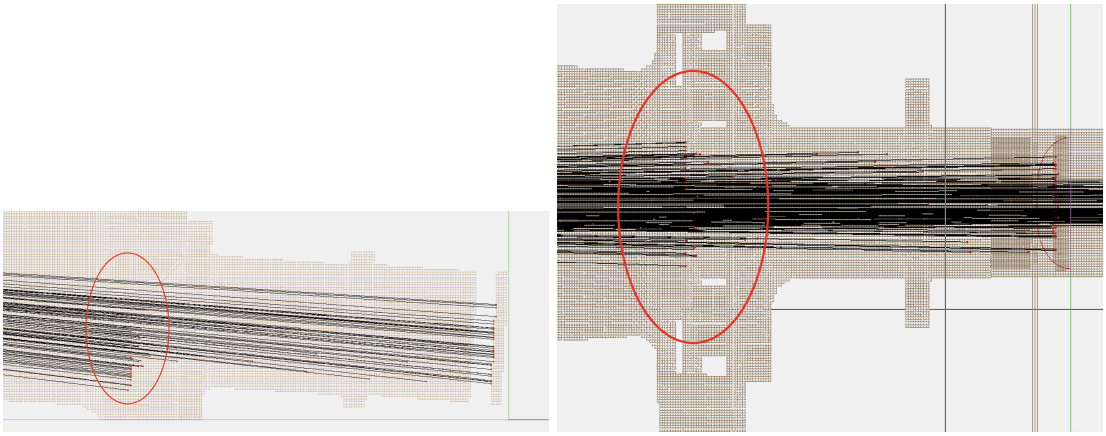

(a) (b)

Figure 14: The trajectories of some ions using the optimised voltage set from two perspectives. Numerous ions do not reach the detector but are obstructed beforehand, in contrary to the nominal voltage set. This is most likely due to the previously discussed effects not taken into account by SIMION.

6 Data Analysis

Nearly all of the data analysis was carried out using Python scripts. The data is recorded by the already mentioned software *AcqirisLive* and saved in *.awd* format, which is a fax image format used mainly by older Microsoft Windows operating systems. The saved file comprises of bins, representing time divisions in which the arriving signal was measured, together with the corresponding bin height representing the amplitude of the signal measured. This amplitude consists of a large number of summed up extractions, roughly about 65'000 per round.

The first step is to subtract the background spectrum, which is either a spectrum with the emission current set to $I_{\text{em}} = 0$ µA or a spectrum where the emission current is at the desired value but no gas has been injected. In the first case, the pulser noise and offset are subtracted, while in the second case the chamber background can also be deducted. A demonstration of this procedure is depicted in figure 15. It should be mentioned that despite using the background spectra from before the gas inlet, the peaks from water and nitrogen and their respective fragments could only be reduced but rarely eliminated. This might be attributed to some residual gas in the inlet valve for the gas bottle.

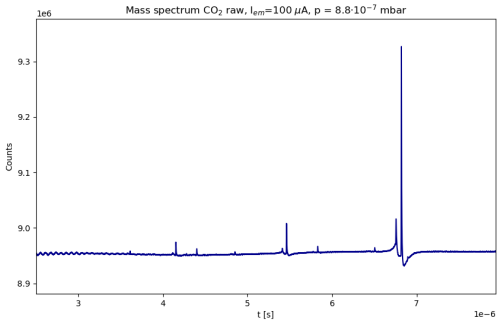

(a) raw spectrum

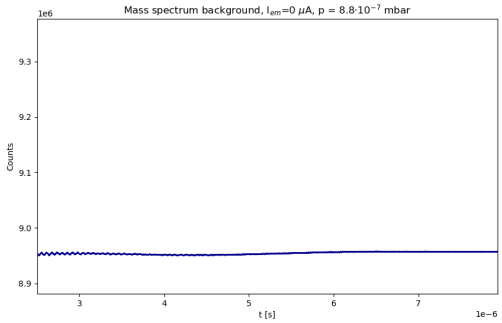

(b) background at $I_{\text{em}} = 0$ µA

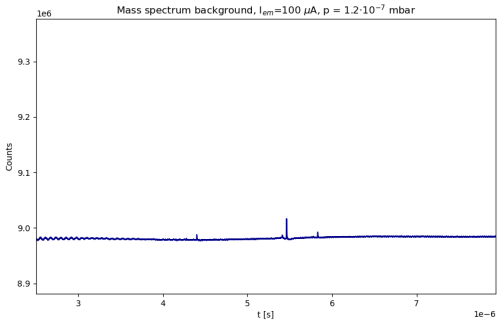

(c) background at $I_{\text{em}} = 100$ µA

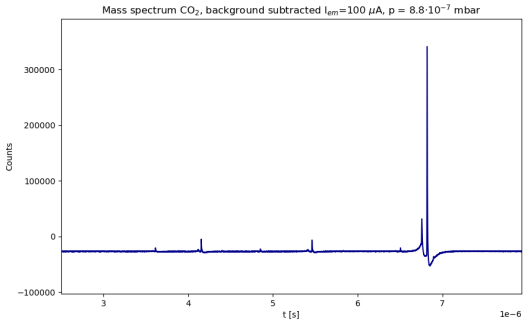

(d) spectrum with background subtracted

Figure 15: Spectra of carbon dioxide measurements. The spectrum in 15a was plotted without any modifications. In 15b, the spectrum was captured prior to turning on the emission current, while the spectrum in 15c was taken before the introduction of CO_2. Subsequently, the final spectrum in 15d was obtained by subtracting the spectrum in 15c from the spectrum in 15a. Significant baseline shift occurred as a result of the subtraction process.

The next step is the calculation of the time-mass conversion parameters, C and t_0, as seen in equation 3. This is done by identifying two signals that are known to belong to a certain ion, such as the water peak or the nitrogen peak, which are almost always present. One such

conversion is shown in figure 16.

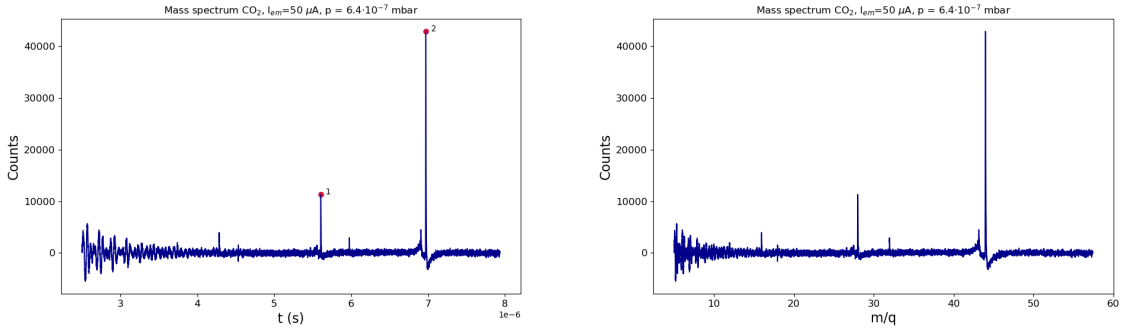

(a) Spectrum before x-axis conversion

(b) Spectrum after x-axis conversion

Figure 16: In figure 16a, two peaks were identified with a prominence exceeding 11'000. Based on the gas that was introduced, the larger of the two peaks can be attributed to CO_2 with m/z 44. The second peak, referred to as peak 1 in the plot, could be due to the presence of nitrogen with m/z 28, as the chamber had recently been sealed and not thoroughly pumped of nitrogen, or could also result from CO, a fragment from CO_2. The values for the parameters were calculated as $t_0 = 2.13 \cdot 10^{-7}$ s and $C = 1.02 \cdot 10^{-6} \frac{\text{Da}}{\text{C·s}}$. In 16b we see the same spectrum but with the mass-to-charge x-axis.

After setting the x-axis, the next step is to use either the `find_peaks` function from `scipy.signal`, which has already been used to identify two peaks for the axis conversion and automatically identifies the peaks in the spectrum with a given prominence, or to manually search for the expected molecule-ions along with their fragments and isotopes at the predicted m/z.
Prior to fitting a function, it is helpful to include the `BaselineRemoval` function, and to use the `Zhangfit` function to remove any noise coming from the electronics.
Now, the final step is to fit an exponentially modified Gaussian (EMG) to the identified peaks and calculate the area under the function to facilitate abundance comparison. Figure 17 shows the whole process.
The precise form of the function for the EMG is

$$f(x;\mu,\sigma,\lambda) = \frac{\lambda}{2} e^{\frac{\lambda}{2}(2\mu+\lambda\sigma^2-2x)} \operatorname{erfc}\left(\frac{\mu+\lambda\sigma^2-x}{\sqrt{2}\sigma}\right) \tag{13}$$

where erfc(X) is the complementary error function defined as

$$\begin{aligned} \operatorname{erfc}(x) &= 1 - \operatorname{erf}(x) \\ &= \frac{2}{\sqrt{\pi}} \int_x^\infty e^{-t^2} dt. \end{aligned} \tag{14}$$

This function is obtained by convolving the probability density functions for the normal and exponential distributions.
The uncertainty for the heights of the peaks would be

$$\sigma_{\text{height}} = \sqrt{h_{\max}} \tag{15}$$

and the uncertainty for the areas would be

$$\sigma_{\text{area}} = \frac{1}{\sqrt{A}}. \tag{16}$$

However, it is not currently known how many signal counts correspond to how many ions at this stage of development. Therefore, this should not be assumed. To determine this, a calibration measurement with galactic cosmic rays would need to be conducted and evaluated to determine the amount of ADC signal produced by a single ion. If the ADC signal count were to be used, the Poissonian error would be overestimated since the MPC amplifies the original signal generated by one ion.

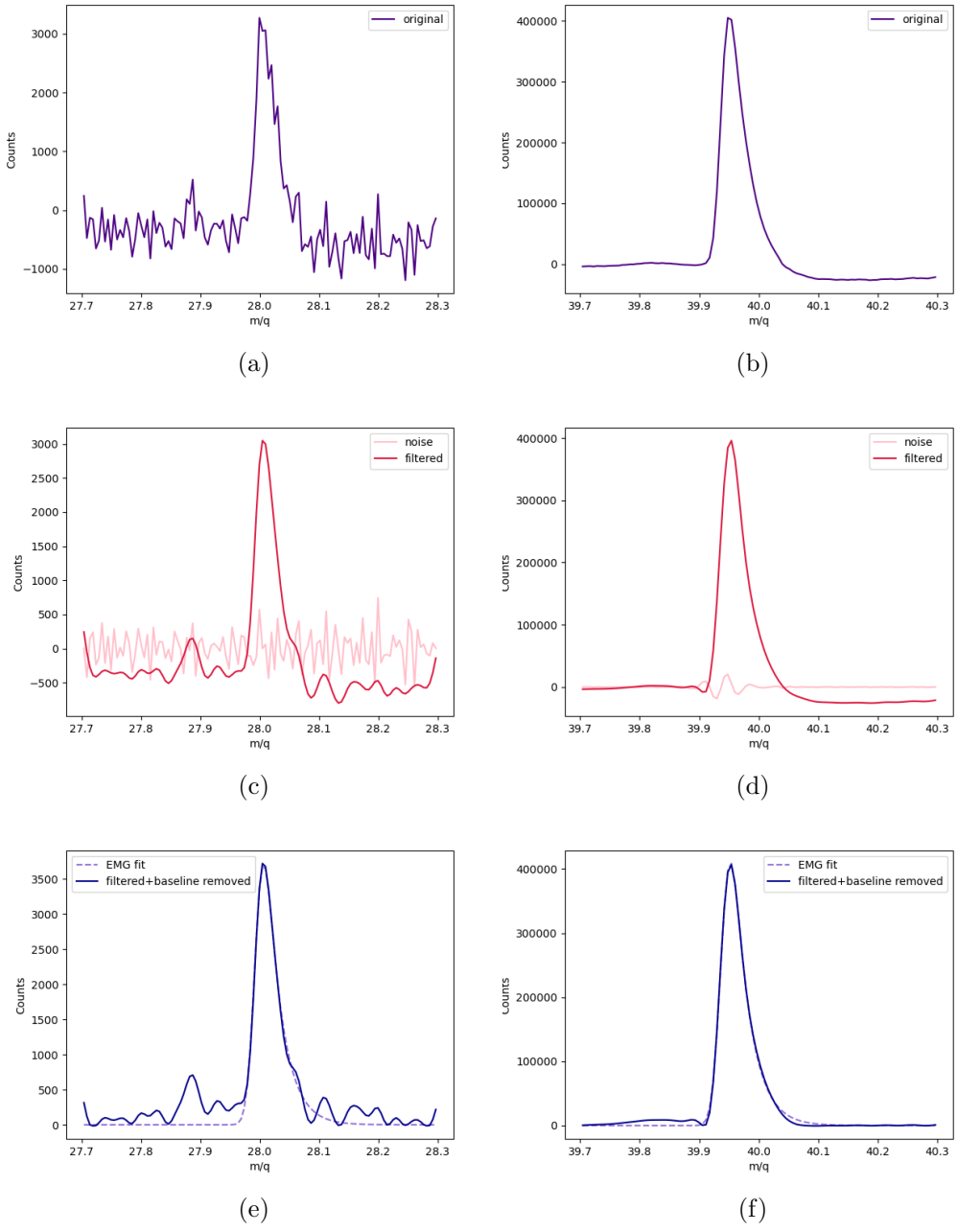

Figure 17: The six images depict the peak shape refinement procedure using two examples with different prominences. The raw peaks are visible in (a) and (b) and were retrieved from the measured spectrum of argon, where m/z 40 is the nominal peak and m/z 28 belongs to nitrogen. In (c) and (d), noise has been eliminated from the peak. The baseline has been removed in (e) and (f), leading to the final EMG fit.

7 Fragmentation Patterns

To verify the expected resolution, abundance accuracies and pressure dependencies of the MANiaC SHU, two gases were chosen to analyse the fragmentation pattern and isotope distribution: methane (CH_4) and xenon (Xe).
Methane was particularly interesting, as one fragment is obtained for each substracted hydrogen atom ($[CH_3]^+$, $[CH_2]^+$, $[CH_1]^+$, $[C]^+$) aside from the parent ion $[CH_4]^+$. The intriguing aspect about xenon is that it has many isotopes in higher mass ranges that had not been tested for our MS, i.e. at m/z around 124-136.
In order to capture these particular masses, the data storage in the *AcqirisLive* data acquisition software had to be changed from 20'000 to 50'000 samples in order to collect signals over longer flight times.

7.1 Methane

When recording spectra a comparison with NIST data [21] would normally be carried out as they have an extensive library of EI-MS spectra.
Of the 6 expected peaks, all were detected, with two additional peaks at m/z 18 and 28 due to water and nitrogen residues.
The measured signal heights and areas show a consistent ranking pattern when compared with the expected NIST abundances, as shown in table 2. There are variations in the values, but the peak order of the heights and areas remain the same. A comparison of the expected and measured spectra can be seen in figure 18.

Table 2: Relative abundances of the methane measurement at $p = 9.0{\cdot}10^{-7}$ mbar.

m/z	**Rel. height [%]**	**Rel. area [%]**	**NIST [%]**	**Resolution**
12	1.52	2.04	3.80	315
13	4.63	4.70	10.69	463
14	10.75	11.39	20.42	480
15	77.06	76.01	88.80	546
16	100.00	100.00	100.00	579
17	1.34	2.32	1.64	279

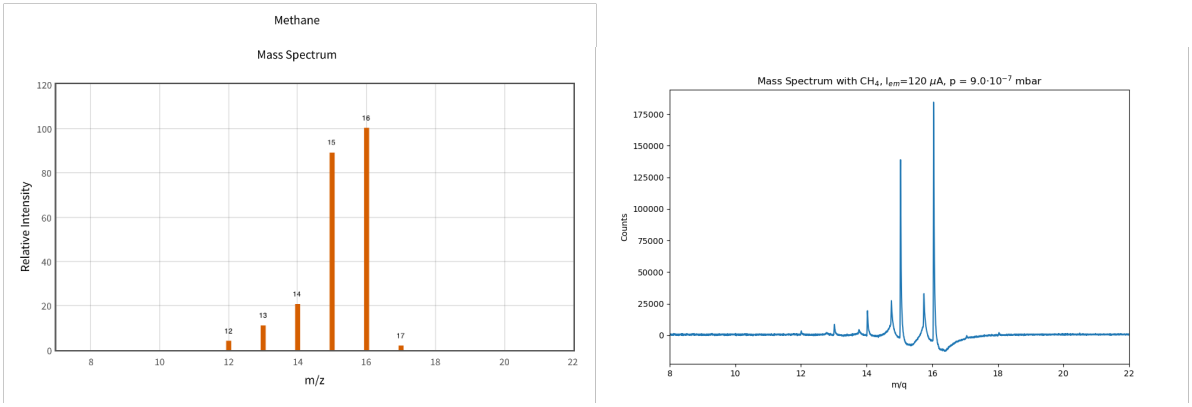

(a) NIST spectrum of methane

(b) Measured spectrum of methane

Figure 18: Comparison between NIST spectrum [21] and measured spectrum of methane at pressure of $p = 9.0{\cdot}10^{-7}$ mbar and $I_{\text{em}} = 120$ µA

A further analysis was made between the measurements where different amounts of methane were introduced into the chamber. From the measured peaks it can be seen in figure 19 that measurements with different amounts (considering pressure) recovered the same fragmentation patterns. The only peaks that changed in relative abundance were the nitrogen and water peaks. Their abundance increased or decreased depending on whether more or less methane was introduced.

Another comparison was made between the spectra where the background was made with an emission current of $I_{\text{em}} = 0$ µA and one where the emission current was the same as in the methane measurements just before the gas was injected. The relative abundances of water and nitrogen were visibly reduced, as can be seen in the figure 20, while the corresponding methane signals remained the same.

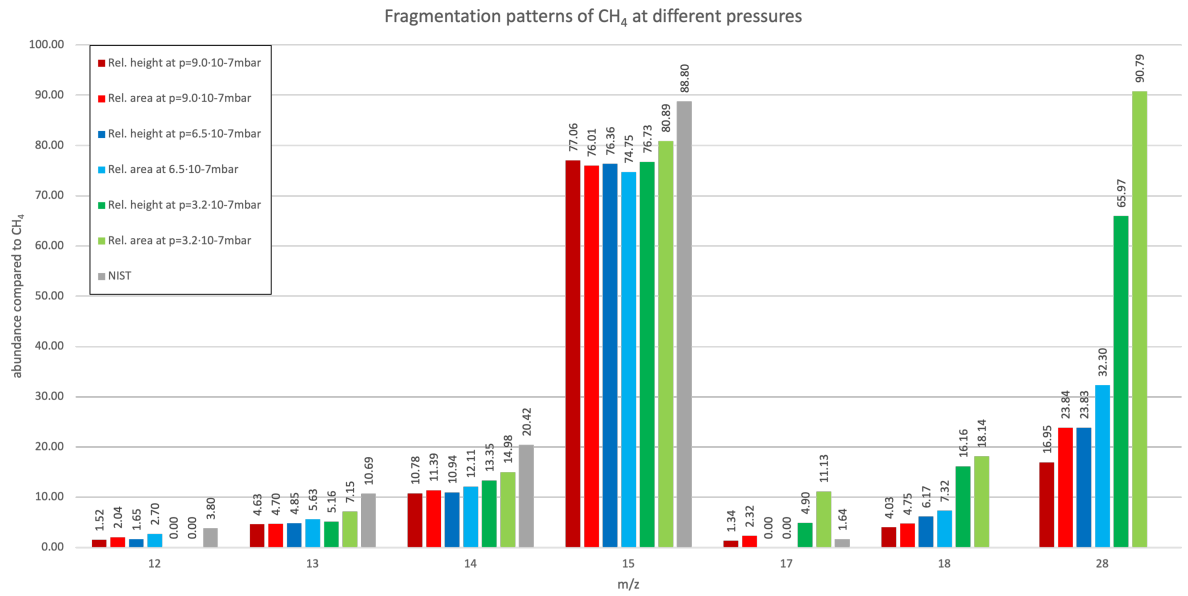

Figure 19: Relative abundances of fragments and isotopes of the methane measurements compared to the main peak at m/z 16 at different pressures. Note that the amount injected does not change the relative abundance (except for m/z 18 and 28).

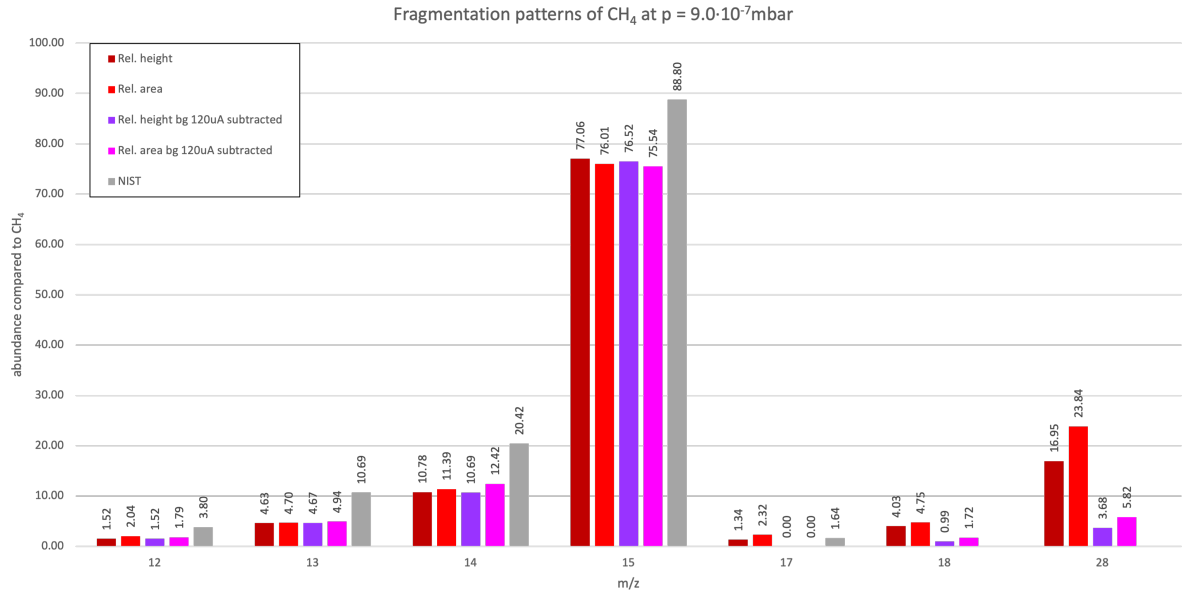

Figure 20: Relative abundances of fragments and isotopes of the methane measurement compared to the main peak at m/z 16 with two different backgrounds subtracted. The abundances do not change except for the peaks at m/z 18 and 28, which are considered to be residual gases anyway.

7.2 Xenon

Xenon has 7 stable isotopes with m/z of 126, 128, 129, 130, 131, 132 and 134 as well as two isotopes with very long half lives, 124 and 136 [22]. Of those 9 isotopes, 7 were detected together with 3 doubly charged isotopes of 132, 134 and 136. Those with a relative abundance of less than 3% of the highest peak at m/z 132 according to NIST were not detected. Similar to the methane measurements, additional peaks were identified at m/z 18 and 28, which can be attributed to water and nitrogen.
The relative abundances were comparable to what could be expected from NIST (see table 3 and figure 21) and there was no pressure dependence detected, as can be seen in figure 22, while subtraction of the background at $I_{\text{em}} = 120$ µA succeeded in reducing the amount of residual gases as visualised in figure 23.

Table 3: Relative abundances of the xenon measurement at $p = 9.0{\cdot}10^{-7}$ mbar. For peaks with m/z values below 124, a considerable difference was observed between the relative height and relative area, particularly for the lighter peaks. This may be attributed to the fact that signals from lighter peaks are commonly narrower and taller, as demonstrated in Figure 24. Furthermore, since the relative heights were normalised to the peak at m/z 132, this trend becomes more pronounced in the lighter peaks.

m/z	**Rel. height [%]**	**Rel. area [%]**	**NIST [%]**	**Resolution**
61	-	-	0.01	-
64	-	-	1.32	-
65	-	-	2.93	-
66	22.80	12.01	17.76	861
67	9.50	5.24	6.90	832
68	7.86	5.07	6.05	721
124	-	-	0.35	-
126	-	-	0.34	-
128	8.88	8.75	7.05	816
129	97.88	95.79	98.41	908
130	13.60	11.79	15.20	1027
131	77.31	73.82	79.40	941
132	100.00	100.00	100.00	907
134	39.19	40.28	37.83	891
136	32.49	33.93	31.97	880

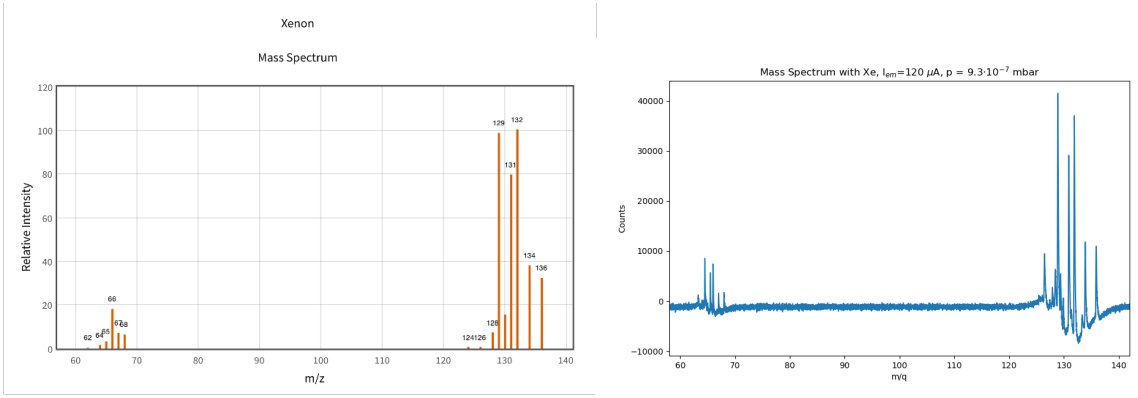

(a) NIST spectrum of xenon (b) measured spectrum of xenon

Figure 21: Comparison between NIST spectrum [21] and measured spectrum of xenon at pressure of p = 9.3·10^{-7} mbar and I_{em} = 120 µA

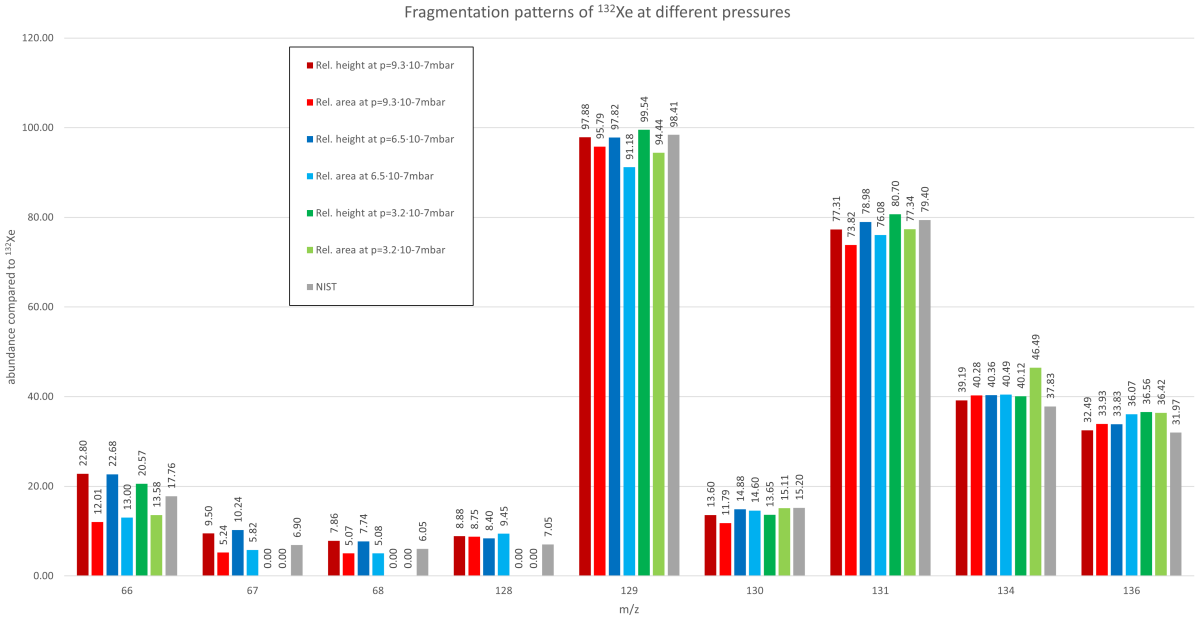

Figure 22: Relative abundances of fragments and isotopes of the xenon measurements compared to the main peak at m/z 132 at different pressures. Note that the amount injected does not change the fragmentation pattern.

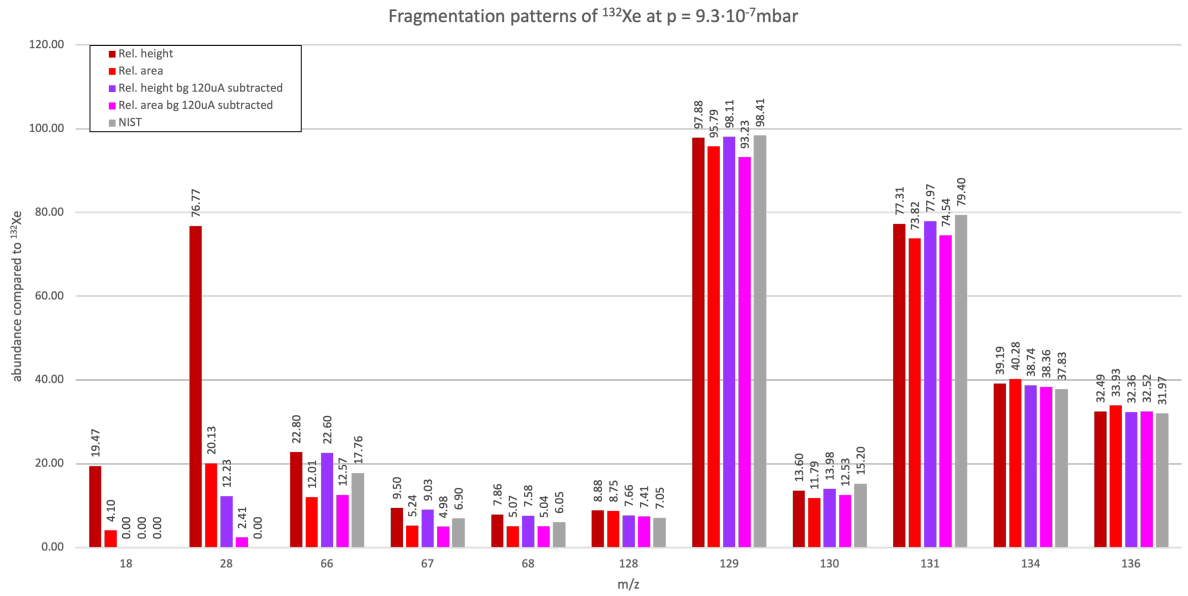

Figure 23: Relative abundances of fragments and isotopes of the xenon measurement compared to the main peak at m/z 132 with two different backgrounds subtracted. The abundances do not change except for the peaks at m/z 18 and 28, which are again considered to be residual gases anyway.

An effect that started to become more apparent in these measurements is the widening of the peak shape with higher masses (see again figure 24) . This is to be expected and the resolution will stay more or less constant as ΔM its proportionally increasing to M as explained in sub-subsection 2.4.3.
Furthermore it should be noted that the measured mass-per-charge ratio of the xenon isotopes turned out to be somewhat lower than the integer values, which was also anticipated [22].

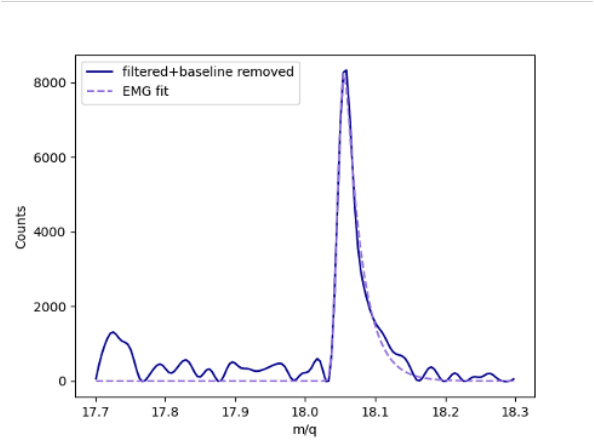

(a) peak at m/z 18

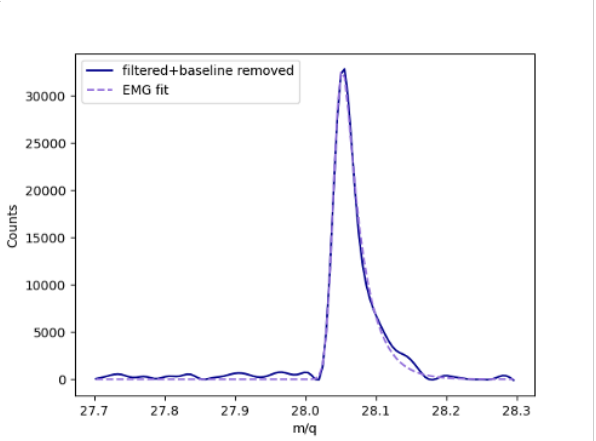

(b) peak at m/z 28

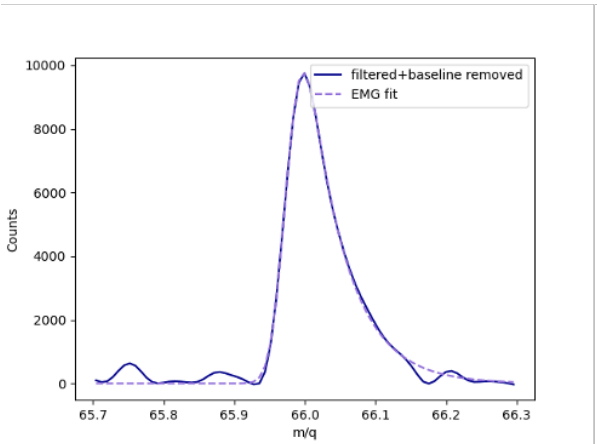

(c) peak at m/z 66

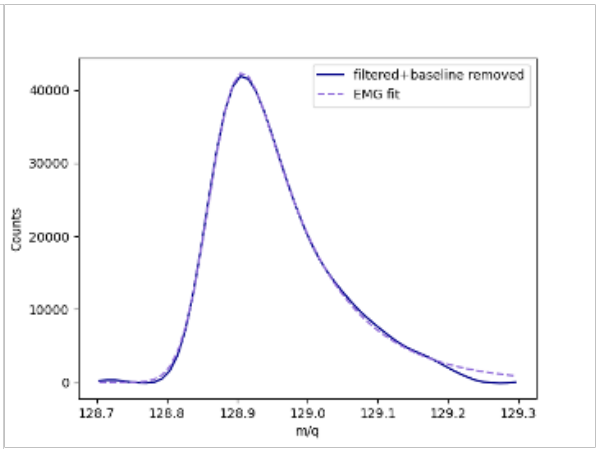

(d) peak at m/z 129

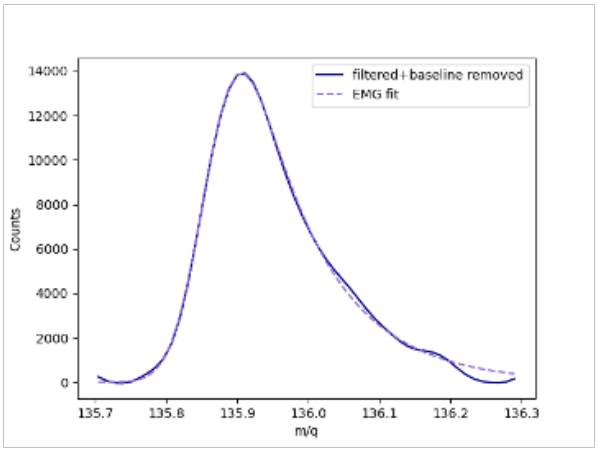

(e) peak at m/z 136

Figure 24: Selected processed peaks from the xenon measurements at $p = 9.3{\cdot}10^{-7}$ mbar and $I_{\text{em}} = 120$ µA. The widening of the peak becomes more apparent with higher masses. The resolution stays more or less constant at higher masses (see table 3.

8 Comparison of CO_2 Signals

The ions are extracted from the ion source region into the drift region by a pulsed extraction potential. To maximise resolution, shortening the pulse rise time is advised. While the pulse amplitude initially appears rectangular, with closer inspection, it displays a finite slope to the rise. By maximising this gradient but at the same time preventing overshooting of the desired voltage, the period for removing ions from the ion extraction zone reduces, resulting in sharper peaks due to reduced delays between ion acceleration from different parts of the ion source. In essence one provides a sharp starting point for the ions when the ramp is infinitely short. One possibility for shortening the rise time is to decrease the capacity by using a shorter cable. Such a measure was adopted for the MANiaC SHU prototype. To compare the increase in resolution, measurements taken before and after were compared. The results are illustrated in figure 25 with some example signals. As expected, there was an increase in resolution and area as well as amplitude. Halving the rise time from 10.9 ns to 5.20 ns doubled the resolution in most cases. It may appear that there is an anti-linear relationship, but conclusive statements cannot be made until further testing is conducted. In terms of the relative abundance, the signals moved closer to the reference numbers after the modification in most cases (see table 4). The abundances of lower mass signals, such as m/z 12 and 16, deviated slightly. However, it was consistently observed that the masses falling within the lower range around m/z produced a signal lower than the NIST prediction.
In contrast to the positive effect this change had on the resolution and accuracy of the signal, it did cause an instability problem where the signal height and area would change over the course of a day, which was not desirable. Reverting to the previous setup resulted in a more stable signal. This phenomenon requires further investigation and attention.

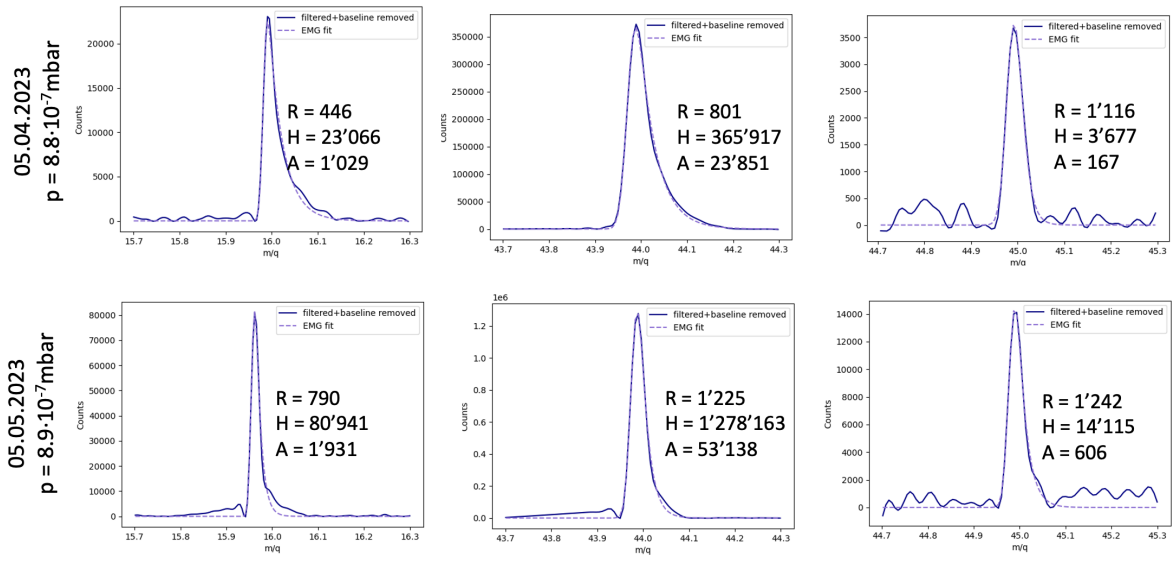

Figure 25: Comparison of resolution area and height of the carbon dioxide measurements acquired with a larger pulse rise time (top panel) and a shorter pulse rise time (bottom panel). The shorter pulse rise time leads to more compact ion packets resulting in a sharper peak and higher mass resolution.

Table 4: Relative abundances of the carbon dioxide measurements at $p = 8.8{\cdot}10^{-7}$ mbar (05.04.23) and $p = 8.9{\cdot}10^{-7}$ mbar (05.05.23) with shortened pulser cable.

m/z	**Rel. area[%] 05.04.23**	**Rel. area [%] 05.05.23**	**NIST [%]**
12	0.33	0.71	8.71
16	2.55	3.35	9.61
22	0.33	0.83	1.90
28	3.41	5.29	9.81
29	-	-	0.10
44	100	100	100.00
45	0.45	1.11	1.20
46	-	0.46	0.40

9 Emission Current Dependence

Augmenting the emission current usually leads to an increase in signal height. This occurs because more electrons are emitted from the filament, which raises the probability of ionisation for any given neutral species. To validate and examine this phenomenon, experiments were conducted in which selected gas peaks were observed under varying emission currents. The majority of gases and peaks display a linear relationship. Neon and carbon monoxide, however, exhibit irregularities, which may be due to specific molecular effects or may be outliers in the measurements. Figure 26 displays the results obtained.

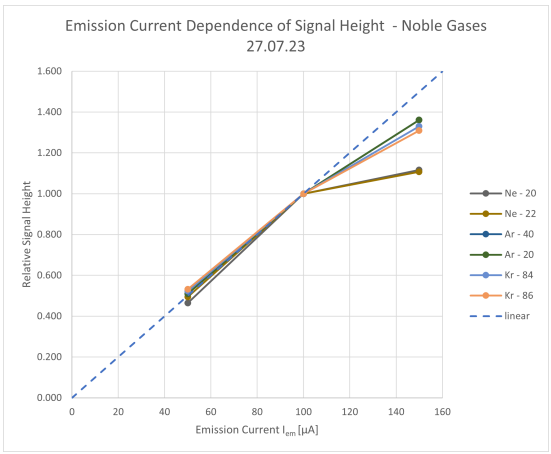

(a) Emission dependence for neon, argon and krypton

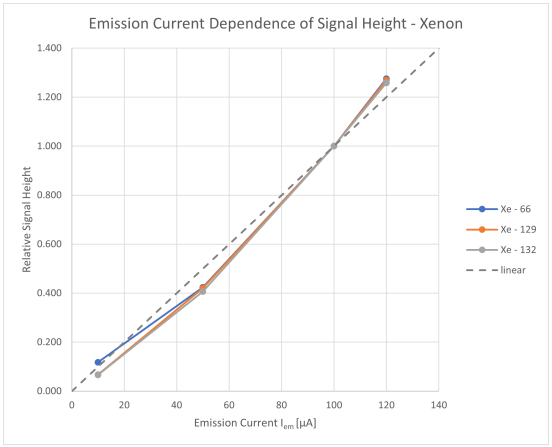

(b) Emission dependence for xenon

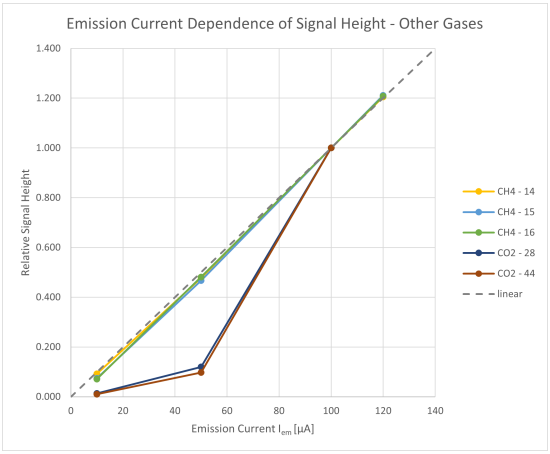

(c) Emission dependence for methane and carbon dioxide

Figure 26: The relationship between signal height and filament current emission was measured with various gases. Two or three peaks were selected for each gas to compare their maximum heights at varying currents. The signal height is relative to the signal height measured with I_{em}= 100 µA.

10 Sensitivity Relations with Noble Gases

When comparing the abundances of different gases and molecules, it is crucial to consider their varying sensitivities. The signal detected by a specific quantity of one molecule will differ from that of an equivalent quantity of a different one. This so-called sensitivity of a MS depends on the already mentioned cross section and the detector efficiency or yield, the emission of the filament and the transmission of the instrument.
It is defined as follows:

$$S_{\text{ion}} = \frac{I_{\text{ion}}}{\rho \cdot I_{\text{em}}} \tag{17}$$

where S_{ion} is in cm^3. For this work, the relative sensitivities of the gases to each other will be considered. I_{em} represents the emission current in amperes, while ρ is measured in cm^{-3} and I_{ion} represents the current detected for the ion. Since the current detected per ion is not known but only the relative signal count for the masses, the formula had to be adapted:

$$S_{\text{ion, rel}} = \frac{C_{\text{ADC}}}{\rho \cdot I_{\text{em}}} \tag{18}$$

Here C_{ADC} is now the area count for each signal peak measured. The signal comprises either only the parent ion or the parent ion together with its fragments, isotopes, and doubly charged particles. To obtain the density of ions ρ from the data, the relationship between density, pressure, and volume was utilised, as expressed by the equation:

$$pV = Nk_BT \quad \rightarrow \quad \rho = \frac{N}{V} = \frac{p}{k_BT}. \tag{19}$$

The pressure, measured in pascals, was used in conjunction with the Boltzmann constant ($1.38 \cdot 10^{-23}$ J/K) and the temperature, taken to be room temperature $T = (293 \pm 5)$ K, to find the density.
To ascertain sensitivity, noble gases are the optimal candidates to use due to their lack of fragmentation and the sole presence of doubly ionised particles and isotopes, reducing uncertainties. There were two rounds of measurements for the sensitivity relations. For the first experiment all of the noble gases were used and their sensitivities were determined. As a matter of interest, the sensitivities of other measurements, which were not recorded on the same day, were taken into account to see if there was any consistency. The results can be seen in table 5.

In the case of xenon and carbon dioxide we see that the results are not consistent over several measurements taken on different days. This could be explained by the different voltage sets used as well as other settings that had been changed in the meantime. Based on this result, it was decided to repeat the measurements with all the gases present in the laboratory on the same day in order to have comparable sensitivities.
During the second round of measurements, all gases present in the laboratory were evaluated, non-noble gases included, and the signal was measured at three different pressures (approximately $3 \cdot 10^{-7}$ mbar, $8 \cdot 10^{-7}$ mbar, and $3 \cdot 10^{-6}$ mbar). From these measurements, the average sensitivity was calculated. As all the gases were measured on the same day, there would have been no variation in sensitivities due to the differences in voltage sets. The results are presented in table 6.

Table 5: Results from the first analysis consisting of the noble gases measurements together with some past measurements of other gases. The relative sensitivities with product ions include all the peaks that are related to the molecule while the relative sensitivities with only parent ion contain only the area of the main peak or the main isotope in the case of noble gases. The significant difference in sensitivity for xenon is due to the many isotopes of xenon, whereas for ethane it is due to its many fragments.

Date	**Gas**	**Relative Sensitivities (with product ions)**	**Relative Sensitivities (only parent ion)**
05/04/2023	CO_2	3.36	3.14
19/04/2023	CH_4	1.25	0.64
	Xe	3.04	0.80
05/05/2023	CO_2	7.57	6.77
22/06/2023	N_2	9.35	8.85
	CO	8.46	8.08
	C_2H_4	8.60	3.50
27/07/2023	Ne	2.70	2.44
	Ar	4.03	3.82
	Kr	4.69	2.49
	Xe	4.01	1.16

Table 6: Results from the second analysis comprise all gases that were present in the lab. Like the preceding table, this table has a sensitivity column that relates the fragments, isotopes, and doubly charged ions with each other. In addition, there is a column displaying the signal from the nominal peak or the main isotope in case of noble gases.

Gas	**Relative Sensitivities (with product ions)**	**Relative Sensitivities (only parent ion)**
Ne	2.32	2.10
Ar	3.63	3.47
Kr	4.05	2.14
Xe	4.16	1.07
C_2H_4	2.76	1.13
CH_4	2.16	1.08
N_2	2.74	2.59
CO	2.57	2.44
CO_2	4.81	3.65

Upon comparing the two tables, we observe that there were no significant changes in noble gas sensitivities concerning each other since the noble gases were measured on the same day. The same applies to the m/z 28 gases nitrogen, carbon monoxide and ethylene. However, there were notable differences in the relative sensitivities between the gases measured on different days and the sensitivities measured on the same day due to the use of different voltage settings which has multiple effects. For one, some voltage sets have higher resolutions and lead to higher accuracies in the determination of the signal area. Second, a new voltage set may result in slightly different trajectories for the ions, to which some may respond better or worse. For future abundance measurements between two different gases, it is recommended to either determine the sensitivities on the same day or with the same voltage set or an even simple alternative would be to use a reference gas like nitrogen which is then used to normalise the different measurements.

11 Gas Mixture with m/z 28

Identifying molecules using a MS is not always straightforward, as every molecule may not have a unique m/z value. This is especially true for larger organic molecules where the likelihood of two molecules having the same m/z increases. To investigate this scenario, three gases with an m/z of 28 were chosen: nitrogen (N_2), ethylene (C_2H_4), and carbon monoxide (CO). The objective was to determine if their abundances could still be identified despite sharing the same m/z value. Initially, each gas would be measured individually to determine the abundances of its fragments and isotopes. Subsequently, a gas mixture with a 1:1:1 ratio of these gases was introduced into the chamber. The central objective was to examine the spectra of the gas mixture and try to reconstruct the ratio using different methods.

11.1 Area Subtraction

The initial and intuitive approach was to determine the contribution of each molecule to the m/z 28 peak by examining their respective characteristic peaks. Upon reviewing table 7, it becomes apparent that m/z 16 is specific to carbon monoxide and belongs to its $[^{16}]O^+$-fragment, whereas m/z 13, 15, 25, 26, and 27 are unique to ethylene; nitrogen lacks any distinct peak in this mixture. Upon review of the table one might notice some missing fragments like $[^{15}N]^+$ from N_2 considering at m/z 29 there is a signal detected which comes from $[^{15}N^{14}N]^+$. Further there should be $[^{13}C]^+$ from $[^{13}CO]^+$.

Table 7: The appearances of peaks in the gases were measured. A peak distinguishing carbon monoxide from others was observed at m/z 16, while m/z 15, 24, 25, 26, and 27 were identified as characteristic peaks for ethylene.

m/z	**in N_2**	**in CO**	**in C_2H_4**
12		x	x
13			x
14	x	x	x
15			x
16		x	
24			x
25			x
26			x
27			x
28	x	x	x
29	x	x	x
30		x	

The approach taken was to determine the area of m/z 16 and then calculate and subtract the expected areas of all the other carbon monoxide peaks, after the subtraction of the chamber background signal, which includes H_2O that fragments into $[O]^+$. Then, for ethylene, the m/z 27 peak was selected as it was the most abundant and therefore had the least uncertainty and the same procedure was applied. For the final subtraction of the nitrogen peak abundances, m/z 14 was selected due to the high abundance of the remaining peak. The resulting abundances are available to view in table 8.

Table 8: The abundance of each gas in the mixture was determined by subtracting the area of the peak m/z 28. To compare the results with other methods, an evaluation method was introduced that produced an artificial spectrum with the identified abundances, which was then compared with the actual spectrum. The smaller the value, the smaller the differences between the two spectra.

Molecule	**Abundances**
C_2H_4	26.8%
CO	27.6%
N_2	32.2%
other	13.4%
Sum of diff	0.068

The outcomes closely match the anticipated 1:1:1 ratio. The reduced amounts of ethylene and carbon monoxide can be explained by increased fragmentation, particularly in the case of ethylene, which could introduce more uncertainty. The residual 13.4% of the region could potentially be accounted for by residual nitrogen that was present but was not fully eliminated by subtraction of the background measurements.
One potential factor that needs consideration are the differences in ionisation cross sections of the molecules. Ethylene, being a larger molecule, has a higher ionisation cross section (refer to table 9). However, the fact that ethylene seems to have the lowest abundance seems to contradict this and does not account for our results.

Table 9: Electron impact ionisation cross sections at an ionisation energy of 70 eV for ethylene, carbon monoxide and molecular nitrogen. The numbers were retrieved from NIST [23].

Molecule	**Cross Sections σ in [Å]**
C_2H_4	5.115
CO	2.516
N_2	2.508

In addition to the ionisation cross section, the relative detection efficiency (also known as yield) is an important factor in signal acquisition. It determines the number of electrons released in an MCP when ions impinge on it. The yield can be calculated by measuring it, as done by Meier and Eberhardt in 1993 ([24]), but it should be noted that the obtained numbers may not fully overlap with MANiaC's configuration. Despite this, they might suggest what the relative yield usually tends to be. The calculated values can be seen in table 10.

Table 10: Yield for the molecules with m/z 28. The numbers were calculated based on yields determined by Meier and Eberhardt [24] with a voltage difference in the MCP of $\Delta V = 2000$ V.

Molecule	**Yield μ**
C_2H_4	0.726
CO	0.748
N_2	1.009

Another way of analysing the relative abundances is to use the previously assessed relative sensitivity, which is also presented in table 11 for all the fragments of the molecules. The

sensitivity considers ionisation cross sections σ, detector yield μ, and transmission τ and is proportional to those:

$$S \propto \sigma \cdot \tau \cdot \mu \tag{20}$$

Transmission was assumed to be more or less the same for all ions. However, this would result in carbon monoxide having the lowest concentrations, whereas nitrogen and ethylene exhibit comparable concentrations, which is not what is observed. Nevertheless, the numbers obtained using the area subtraction method (see again table 8) were not too far off and give a good estimate of the actual ratio of gases that should be in the gas bottle.

Table 11: Sensitivity relations for the molecules at m/z 28 including all fragments, isotopes and doubly charged ions.

Molecule	**Sensitivity relative to CO**
C_2H_4	1.07
CO	1
N_2	1.07

11.2 Least Squares Fitting

This method comprised arranging the fragmentation pattern of each molecule into an array just as follows (rounded to two decimal places for viewing purposes):

$$R = \begin{pmatrix} 12 & 13 & 14 & 15 & 16 & 24 & 25 & 26 & 27 & 28 & 29 & 30 & \\ 0.01 & 0.02 & 0.05 & 0.01 & 0.00 & 0.03 & 0.11 & 0.58 & 0.61 & 1.00 & 0.03 & 0.00 & C_2H_4 \\ 0.02 & 0.00 & 0.00 & 0.00 & 0.02 & 0.00 & 0.00 & 0.00 & 0.00 & 1.00 & 0.01 & 0.00 & CO \\ 0.00 & 0.00 & 0.05 & 0.00 & 0.00 & 0.00 & 0.00 & 0.00 & 0.00 & 1.00 & 0.01 & 0.00 & N_2 \end{pmatrix} \tag{21}$$

Similarly, a separate array was created to store the abundances detected in the gas mixture:

$$M = \begin{pmatrix} 12 & 13 & 14 & 15 & 16 & 24 & 25 & 26 & 27 & 28 & 29 & 30 & \\ 0.01 & 0.01 & 0.03 & 0.00 & 0.00 & 0.01 & 0.02 & 0.15 & 0.16 & 1.00 & 0.02 & 0.00 & \text{gas mix} \end{pmatrix} \tag{22}$$

Subsequently, equation 23 was solved by computing 24 or more explicitly determining the minimum like in 25:

$$R = M\vec{x} \tag{23}$$

$$(R^T R)^{-1} R^T M = \vec{x} \tag{24}$$

$$\vec{x} = \arg\min \left(\sum_{i=1}^{3} R_i x_i - M_i \right)^2 \tag{25}$$

This approach was implemented by utilising least squares solvers on both Python and Excel. In Python the arrays were given just as in 21 and 22 and solved using a linear solver from the `numpy`-library. The Excel approach utilised a solver to determine the ratio producing the minimum difference in sum between the actual spectrum and the generated spectrum. The abundances determined through this approach are presented in the table 12.

Table 12: Abundances of each gas in the gas mixture determined by the least squares method once using Python and once with Excel. To check the accuracy of the results, the sum of the difference of an artificial spectrum compared to the real spectrum was determined.

Molecule	**Least Square (Python)**	**Least Square (Excel)**
C_2H_4	26.7%	26.7%
CO	39.9%	38.9%
N_2	33.9%	34.9%
Sum of diff	0.016	0.015

To improve this method, a penalty function was introduced. This function penalises possibilities where the resulting abundances subtracted from the abundances in the individual gas measurements would be greater than the square root of the average noise level, i.e. the uncertainties in the signal. If this were true, it would assess the result as P, which could lead to a less favourable evaluation of this particular solution:

$$\text{instead of} \quad \vec{x} = \arg\min \left(\sum_{i=1}^{3} R_i x_i - M_i \right)^2$$

$$\text{use} \quad \vec{x} = \begin{cases} P & \text{if} \quad R_i x_i - M_i > \sqrt{\overline{M}} \\ \arg\min \left(\sum_{i=1}^{3} R_i x_i - M_i \right)^2 & \text{else} \end{cases} \tag{26}$$

The results for different penalty numbers can be found in table 13.

Table 13: The abundances of each molecule in the gas mixture were determined using the least squares method and a penalty function. Furthermore, the total difference between the calculated spectra based on these quantities and the actual spectra was computed.

Molecule	**P = 0**	**P = 0.01**	**P = 0.1**	**P = 1**	**P = 2**	**P = 10**
C_2H_4	23.0%	23.2%	24.7%	29.8%	31.2%	32.8%
CO	58.2%	41.3%	38.0%	35.2%	34.4%	33.6%
N_2	18.7%	35.5%	37.3%	35.1%	34.4%	33.6%
Sum of diff	0.076	0.063	0.041	0.053	0.071	0.092

It is observed that the best fitting result, the one with the lowest value of the sum of differences, is found by the simple solver method using Excel. The ratio found in this case is not 1:1:1 but rather 1:1.5:1.3 with C_2H_4:CO:N_2. The findings are comparable in that ethylene has the lowest abundance again, presumably due to increased fragmentation leading to more signal area loss. Carbon monoxide has a higher abundance than nitrogen this time. It is noted that the unassigned area, which constitutes 13.4 % of the total, was predominantly assigned to carbon monoxide in this instance. Either way, the ratio is near the 1:1:1 proportion.

11.3 Fitting Peaks

The final approach tested involved fitting the m/z peak 28 of each molecule into the gas mixture's and recovering the abundances. This method is effective due to the unique m/z values for each molecule, which varies slightly from the nominal mass of 28. The nitrogen peak appeared in our spectrum at m/z 28.006, while the carbon monoxide and ethylene peaks appeared at m/z 27.990

and m/z 28.026 respectively. The findings are illustrated in figure 27. The result is summarised in table 14.

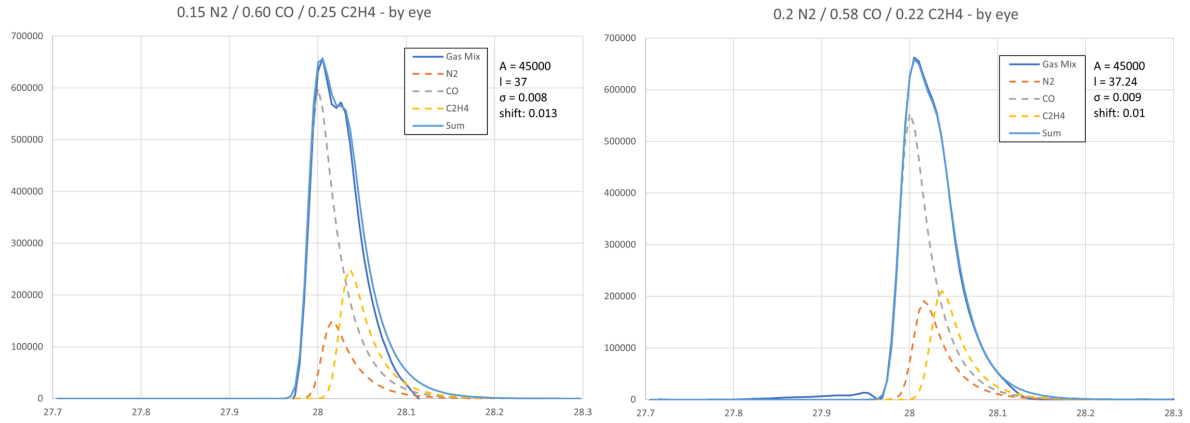

(a) (b)

Figure 27: Fitting three exponentially modified Gaussians to the main peak of the gas mixture, once to the raw signal on the left and once to the processed peak on the right, meaning noise and baseline were removed. The optimal fit was achieved via manual adjustments. It is to be noted that some information is lost when the peak is processed, resulting in the double structure of the peak vanishing.

Table 14: Abundances of each gas in the gas mixture determined by fitting the m/z 28 peaks of each gas into the one of the gas mix.

Molecule	**Abundances (raw)**	**Abundances (processed)**
C_2H_4	15%	20%
CO	50%	58%
N_2	25%	22%
Sum of diff	0.121	0.092

In this method of determining abundances, it is important to consider the contribution of main peak fragmentation to the change in measured abundances. For this work the abundances were usually normalised so that the most abundant peak represented 100%. Another way of representing abundances is as a percentage of the total area of all (fragment) peaks measured. Table 15 illustrates these two methods of abundance representation. In table 16 the areas as percentages of total area are shown for each molecule.

Table 15: Two methods for illustrating the proportions of ions present are demonstrated using the example of ethylene. The numerical values presented are derived from measurements obtained.

Abundances of ethylene		
m/z	**normalised to m/z 28**	**as percentage of total area**
12	1.04%	0.42%
13	2.23%	0.90%
14	4.61%	1.86%
15	1.12%	0.45%
18	0.54%	0.22%
24	3.24%	1.31%
25	11.35%	4.59%
26	57.54%	23.28%
27	61.28%	24.80%
28	100.00%	40.47%
29	2.98%	1.21%
44	1.19%	0.48%

Table 16: Contribution of the total area to the main peak. Due to the extensive fragmentation of ethylene, less than half of the total area is still represented at the parent mass m/z 28.

Gas	**m/z 28 area as percentage of total**
C_2H_4	40.5%
CO	93.2%
N_2	94.3%

The fragmentation of ethylene exceeds that of nitrogen and carbon monoxide, causing the latter to be less abundant when fitting into the parent ion. However, the elevated abundance of carbon monoxide remains unexplained, as it should be roughly equivalent to that of nitrogen.

To consider both the yield and cross section as well, it is possible to utilise the sensitivity previously measured. Since only the m/z 28 peak was analysed, the sensitivity for the main peak provided in table 17 should be used, where only the parent ion was considered for the sensitivity.

Table 17: Sensitivity relations for the molecules at m/z 28 using only their nominal main peak. The sensitivities are in relation to ethylene.

Molecule	**Sensitivity relative to C_2H_4**
C_2H_4	1.00
CO	2.16
N_2	2.29

The determined value of carbon monoxide may be accounted for by its sensitivity. However, if only the sensitivity for the parent ion is considered, it would be expected that there would be

a slightly higher abundance of nitrogen measured. This is not what was determined in table 14 where the level of nitrogen is closer to that of ethylene.

11.4 Summary

After considering all methods employed to determine abundances, the area subtraction method with sensitivity considered came closest to the known ratio. It gave a slightly higher value for nitrogen. Meanwhile, the least square method produced the mass spectrum closest to the one obtained, with a higher abundance of carbon monoxide, followed by nitrogen. Finally, the peak fitting method yielded expected values for ethylene and carbon monoxide when considering sensitivity for the parent ion. However, the value for nitrogen produced a significantly lower outcome.
As there was no consistent pattern of one gas having higher abundance, the minor anomalies cannot be attributed to the mixture in the gas bottle differing from the indicated 1:1:1 ratio.
If back calculations are done using the ionisation cross section and yield, one would expect the values in table 18.

Table 18: By back-calculation and using cross section and detector efficiency, a ratio of 2:1:1.3 for C_2H_4:CO:N_2 is expected when all ions are taken into account. However, based on the sensitivity determined experimentally, the ratio is anticipated to be closer to 1.1:1:1.1. Note that sensitivity in this case takes all ions into account.

Gas	**Ratio**	**Cross Sections σ in [Å]**	**Yield μ**	**Expected Ratio**	**Sensitivity S Ratio**
C_2H_4	1	5.115	0.726	2.0	1.1
CO	1	2.516	0.748	1.0	1.0
N_2	1	2.508	1.009	1.3	1.1

The predicted 2:1:1.3 ratio for C_2H_4:CO:N_2 does not match our measured results, as ethylene consistently had the lowest abundance. However, the sensitivity analysis, which considers both ionisation cross section and detection efficiency, as well as transmission, indicates that the signal from these gases using similar densities will be consistent. This aligns with the observations made using both area abundance and the least square methods. Backcalculating while also taking fragmentation into account leads to the ratios in table 19.

Table 19: Again by back-calculating and using ionisation cross section and detector efficiency as in table 18 but only for the parent peak, a ratio of 1:4.5:3.4 for C_2H_4:CO:N_2 for the area of the m/z 28 peak is expected. The sensitivity for the parent ion shows 1.0:2.2:2.3.

Gas	**Ratio**	**Expected ratio with σ and *yield***	**m/z 28 area of total area**	**Expected Ratio**	**Sensitivity S Ratio**
C_2H_4	1	2.0	40.5%	1.0	1.0
CO	1	1.0	93.2%	4.5	2.2
N_2	1	1.3	94.3%	3.4	2.3

The anticipated ratio indicates that ethylene would produce the lowest signal, as confirmed by the peak fit analysis of m/z 28. Nonetheless, the proportion of carbon monoxide and nitrogen is significantly higher than the one determined by peak fit or expected from the sensitivity measurements. Taking all factors into account, the recommended approach for examining abundances would likely involve area subtraction, alongside a cross-check of the least square technique.

The sensitivities measured were not sufficient to explain some of the discrepancies, but they may still be helpful as they give closer results than considering ionisation cross section and detector efficiency separately. In addition, conducting another experiment with a gas mixture of known ratio is advisable, which was attempted and documented in the next section.

12 Propane & Ethylene Abundances

To test the applied methods for abundance determination in section 11, a slight change to the gas inlet system was made, that allowed to produce gas mixtures. There were two gas bottle inlets attached to a junction piece. Prior to entering the junction, the gases were introduced to a connection piece of equal volume. By adjusting the pressure in that volume, any desired ratio could be achieved. For this experiment, a 1:1 mixture of ethylene (C_2H_4) and propane (C_3H_8) was to be created by releasing 1 bar pressure of each into their respective connecting pieces and then introducing them into the junction. This pair of gases is of particular interest for studying and determining abundances, as the fragments of propane coincide with those of ethylene.
Analysis of the resulting abundances was conducted using previously established methods. Owing to the difference in mass of the parent peak of the molecules, the peaks fitting method was not utilised. Results are given in tables 20 and 21.

Table 20: Abundances of propane and ethylene in the gas mixture determined by area subtraction.

Molecule	**Area Subtraction**
C_2H_4	10.1%
C_3H_8	89.9%
Sum of diff	0.249

Table 21: Abundances of propane and ethylene in the gas mixture determined by the least squares method once using Excel.

Molecule	**Least Square (Excel)**
C_2H_4	2.1%
C_3H_8	97.9%
Sum of diff	0.079

It was observed that the desired 1:1 ratio was not achieved and the content of propane was found to be significantly higher than anticipated. The ratio is unexplained by the sensitivity relation between the two gases (see table 22) which would expect an almost 1:1 ratio. Further checking of the spectra lead to the same conclusion as can be seen in figure 28.
Possible explanations include insufficient time for the valve to evacuate and residual gas, as C_3H_8 was the gas previously measured separately. Since this was the first instance of using the valve in this manner, further experimentation may be necessary to become more familiar with it and obtain the expected results.

Table 22: Sensitivity measurements for ethylene and propane. Note that for this sensitivity all peaks, parent and product ions, were considered

Molecule	**Sensitivity relative to C_2H_4**
C_2H_4	1.00
C_3H_8	1.03

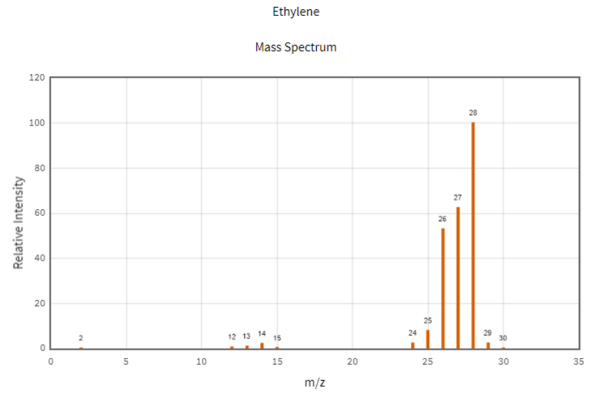

(a) NIST spectrum of ethylene.

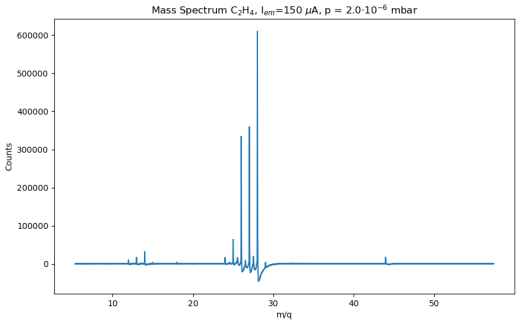

(b) Spectrum of ethlyene.

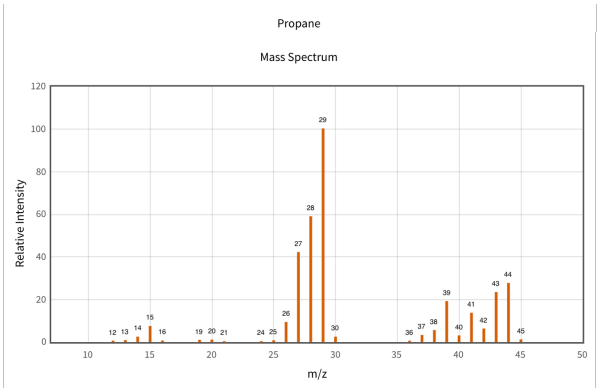

(c) NIST spectrum of propane.

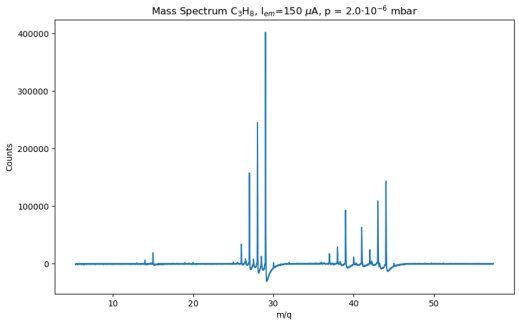

(d) Spectrum of propane.

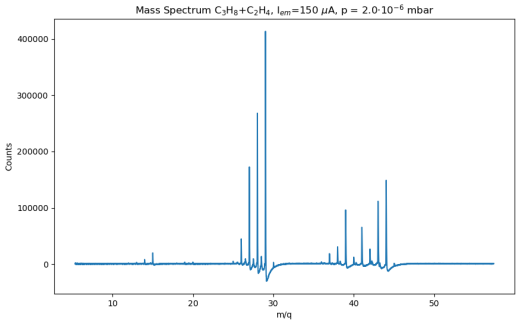

(e) Mixture.

Figure 28: The top panel displays the expected spectrum of ethylene alongside the measured spectrum. The middle panel shows the same for propane. The bottom spectrum is the mixture of both gases, which appears almost identical to the measured propane spectrum.

Part III
Conclusions and Outlook

The aim of this thesis was to carry out tests using different gases with different mass ranges, isotope patterns and fragmentation behaviour to test whether the MANiaC SHU prototype was able to recover the expected results.

It was observed that for almost all gases the anticipated spectra were measured and gave comparable results to the literature values. Some of the signals at lower mass-to-charge ratios exhibited abundances that were below those expected, but this effect can be corrected by proper calibration. No irregularities were detected on this matter.

It was further confirmed that the quantity of gas injected (measured by the pressure reading) did not alter the abundance ratios between the parent peak and its minor isotope and fragments. By subtracting the background at the same emission current as the main measurement, one can achieve improved background subtraction of residual gases and substances such as nitrogen and water.

To enhance peak resolution, it is possible to modify the pulser cable to reduce its capacity. Subsequent stability measurements revealed that this may cause signal instability over time, resulting in fluctuations in signal height and area within a day. This is suboptimal given the planned duration of the flyby, potentially leading to inaccurate results. Further work on the pulser and additional experiments are necessary to stabilise the signal over longer time scales.

The signal height demonstrated a linear relationship with the emission current of the filament across multiple gases. This linear variation in peak heights was observed among different measurements, gases and peaks.

The abundance measurements, in conjunction with the sensitivity measurements, have produced inconclusive findings where the anticipated ratios were not completely retrieved. To reach a definite conclusion, further experiments using other gas bottle mixtures and new custom blends with the valve installed would be necessary, to check how accurate of a result can be achieved.

Overall, despite some discrepancies in the abundance measurements, the majority of the outcomes were as anticipated. The findings indicate that the MANiaC SHU prototype performs as expected and that the mass spectra for all ten gases can be obtained with a satisfying mass resolution.

Part IV
Appendix

References

[1] A. Fraknoi, D. Morrison, and S. C. Wolff, *Astronomy*, OCLC: 961476196 (OpenStax College, Rice University, Houston, Texas, 2016).

[2] F. L. Whipple, "A comet model. i. the acceleration of comet encke", The Astrophysical Journal **111**, ADS Bibcode: 1950ApJ...111..375W, 375–394 (1950).

[3] *History of cometary missions*, https://www.esa.int/Science_Exploration/Space_Science/Rosetta/History_of_cometary_missions (visited on 09/04/2023).

[4] *Touchdown! rosetta's philae probe lands on comet*, https://www.esa.int/Science_Exploration/Space_Science/Rosetta/Touchdown%21_Rosetta_s_Philae_probe_lands_on_comet (visited on 09/04/2023).

[5] D. K. Yeomans, J. Rahe, and R. S. Freitag, "The history of comet halley", Journal of the Royal Astronomical Society of Canada **80**, ADS Bibcode: 1986JRASC..80...62Y, 62–86 (1986).

[6] E. Halley, J. Senex, and d. D. Burndy Library, *A synopsis of the astronomy of comets*, in collab. with Smithsonian Libraries (London : Printed for John Senex ..., 1705), 60 pp.

[7] W. F. Huebner, J. Benkhoff, M.-T. Capria, A. Coradini, C. De Sanctis, R. Orosei, and D. Prialnik, *Heat and gas diffusion in comet nuclei*, Publication Title: Heat and Gas Diffusion in Comet Nuclei ADS Bibcode: 2006hgdc.conf.....H (June 1, 2006).

[8] C. Snodgrass and G. H. Jones, "The european space agency's comet interceptor lies in wait", Nature Communications **10**, 1–4 (2019).

[9] *Comet interceptor - definition study report* (ESA, 2022).

[10] H. Budzikiewicz and M. Schäfer, *Massenspektrometrie: eine einführung*, 6., vollst. überarb. und aktualisierte Aufl (Wiley-VCH, Weinheim, 2012), 222 pp.

[11] E. d. Hoffmann and V. Stroobant, *Mass spectrometry: principles and applications*, 2nd ed (Wiley, Chichester ; New York, 2001), 407 pp.

[12] T. Cornish and W. Bryden, "Miniature time-of-flight mass spectrometer for a field-portable biodetection system", Johns Hopkins APL Tech Digest **20** (1999).

[13] Physikalisches Institut, Universität Bern, Neville Mehta, *MANiaC instrument design and performance report*, 1 (Mar. 17, 2022).

[14] O. B. Chassela, A. Grigoriev, A. Fedorov, N. André, E. Le Comte, and J. Rouzaud, "Thermal characterization of resistance and gain of microchannel plate (MCP) detectors for the JENI experiment", CEAS Space Journal **11**, 597–605 (2019).

[15] *Intro to mass spectrometry*, https://www.orgchemboulder.com/Spectroscopy/MS/abundheavyiso.shtml (visited on 09/06/2023).

[16] V. Gold, ed., *The IUPAC compendium of chemical terminology: the gold book*, 4th ed. (International Union of Pure and Applied Chemistry (IUPAC), Research Triangle Park, NC, 2019).

[17] J. H. Gross, *Massenspektrometrie: spektroskopiekurs kompakt*, Lehrbuch (Springer Spektrum, Berlin, 2019), 131 pp.

[18]B. Pestoni and D. R. Müller, *Pumpstation-5 and SHU user manual* (Mar. 3, 2023).

[19]A. Bieler, "Design of a novel time of flight mass spectrometer and practical application of computer optimization to the development and tuning of mass spectrometers", PhD thesis (Universität Bern, Bern, Mar. 23, 2012), 163 pp.

[20]D. A. Dahl, "Simion for the personal computer in reflection", International Journal of Mass Spectrometry, Volume 200: The state of the field as we move into a new millenium **200**, 3–25 (2000).

[21]N. O. o. D. a. Informatics, *NIST chemistry WebBook*, Publisher: National Institute of Standards and Technology, https://webbook.nist.gov/chemistry/ (visited on 10/07/2023).

[22]F. Kondev, M. Wang, W. Huang, S. Naimi, and G. Audi, "The NUBASE2020 evaluation of nuclear physics properties *", Chinese Physics C **45**, 030001 (2021).

[23]K. Irikura, *Electron-impact cross section for ionization and excitation, NIST standard reference database 107*, 1997.

[24]R. Meier and P. Eberhardt, "Velocity and ion species dependence of the gain of microchannel plates", International Journal of Mass Spectrometry and Ion Processes **123**, 19–27 (1993).